High intensity absorption imaging scheme for a Dysprosium quantum gas

Bachelor's thesis by

Maximilian Emanuel Manfred Kob

Presented to the

University of Stuttgart
5th Institute of Physics

Examiner: Prof. Dr. Tilman Pfau

24th August 2023

Abstract

Absorption imaging is a very common probing technique in experiments with ultracold atoms. It allows the determination of the atom number in a sample. Typically an absorption image is divided by a reference image and the logarithm of the result is taken, yielding the optical densities as described by Beer's law. In this thesis, the effects of saturation on the reconstructed atom number are studied, leading, amongst others, to the modified Lamert-Beer law. A flexible optical setup for imaging atom clouds in a magneto-optic trap as well as Bose-Einstein-condensates is designed, simulated and characterized.

The corrections to the atom number are demonstrated by performing absorption imaging with wavelengths of 421 nm and 626 nm. For the latter transition extended measurements on the power broadening of this transition are done and it is demonstrated, that the variance of the reconstructed atom number can be reduced by introducing a correction factor. Additionally, two EMCCD cameras for use in a quantum gas microscope are characterized.

Zusammenfassung

Absorptionsabbildungen sind eine sehr weit verbreitete Untersuchungstechnik bei Experimenten mit ultrakalten Atomen. Sie erlauben es, die Atomzahl in einer Probe zu bestimmen. Typischerweise wird ein Absorptionsbild und ein Referenzbild durcheinander dividert und der Logarithmus davon berechnet. Dies ergibt, nach dem Lambert-Beer-Gesetz, die optische Dichte. In dieser Arbeit wird der Einfluss von Sättigungseffekten auf die aus der optischen Dichte bestimmte Atomzahl untersuchst, was, unter anderem, auf das modifizierte Lambert-Beer-Gesetz führt. Desweiteren wird ein flexibler optischer Aufbau konstruiert, simuliert und charakterisiert mit dem Atomwolken in magnetooptischen Fallen und auch Bose-Einstein-Kondensate abgebildet werden können.

Die Korrekturen zur bestimmten Atomzahl werden am Beispiel von Abbildungen mit Wellenlängen von 421 nm und 626 nm demonstriert. An letzterem Übergang werden erweiterte Messungen der Leistungsverbreiterung durchgeführt und es wird gezeigt, dass durch Einführung eines Korrekturfaktors die Varianz der rekonstruierten Atomzahl verringert werden kann. Zusätzlich werden zwei EMCCD-Kameras für die Nutzung in einem Quantengasmikroskop charakterisiert.

Ehrenwörtliche Erklärung

Hiermit erkläre ich, dass

- ich diese Arbeit selbständig verfasst habe,
- ich keine anderen als die angegeben Quellen und Hilfsmittel verwendet habe,
- ich alle wörtlich oder sinngemäß aus fremden Werken übernommenen Aussagen als solche gekennzeichnet habe,
- die eingereichte Arbeit weder vollständig noch in wesentlichen Teilen Gegenstand eines anderen Prüfungsverfahren war oder ist,
- der Inhalt des elektronische Exemplars mit dem des Druckexemplars übereinstimmt.

Ort, Datum

Unterschrift

Contents

1 Introduction **1**

2 Theory of optical imaging **3**
2.1 Geometric optics . . . 3
2.2 Airy pattern . . . 4
2.3 Resolving power and diffraction limit . . . 6
2.4 Aberrations . . . 7
2.5 Point-spread-function . . . 8

3 Atom-light interaction **11**
3.1 The two-level atom . . . 11
3.2 Optical Bloch equations . . . 13
3.3 Light absorption . . . 14
3.4 Line widths and power broadening . . . 16
3.5 Imaging noise . . . 18
3.6 Doppler shift and effective scattering cross section . . . 20
3.7 Random walk . . . 22

4 Camera characterisation **25**
4.1 CCD camera characteristics . . . 25
4.1.1 Theoretical background . . . 25
4.1.2 Characterisation of the BFS-U3-63S4M-C camera . . . 27
4.1.3 Characterisation of the BFS-U3-70S7M camera . . . 30
4.2 EMCCD camera characteristics . . . 33
4.2.1 Theoretical background . . . 33
4.2.2 Characterization of the Andor iXon Ultra 888 EMCCD camera . . . 36
4.2.3 Characterization of the Andor iXon 3 EMCCD camera . . . 38

5 Experimental setup **40**
5.1 Requirements and constraints . . . 40
5.2 Imaging setup . . . 41
5.3 Simulation of the optical setup . . . 41
5.4 Characterisation of the magnification and resolution . . . 47
5.5 Characterisation of the magnification in the experiment . . . 49

6 Experimental results **52**
6.1 Imaging with $\lambda = 421\,\mathrm{nm}$ 52
6.2 Imaging with $\lambda = 626\,\mathrm{nm}$ 54
6.2.1 Power-broadening 54
6.2.2 Atom number reconstruction 55

7 Scheme for setting up an absorption imaging system **58**

8 Conclusion & Outlook **60**

9 Bibliography **62**

1 Introduction

In 1924 the article "Plancks Gesetz und Lichtquantenhypothese" by Satyendranath Bose was published, in which quantum statistics were used for the first time [1]. The idea was picked up by Albert Einstein, who expanded on the theory, leading to the Bose-Einstein statistics [2]. One of the key predictions in this theory, the Bose-Einstein condensate (BEC) was experimentally realized in 1995 by C. Wieman and E. Cornell and shortly afterwards by W. Ketterle [3, 4]. They were jointly awarded the Nobel Prize in Physics in 2001 for their discovery [5]. Since then BECs and ultracold quantum gases, in general, have been studied extensively. Dipolar quantum gases have become a topic of particular interest within this field. They interact not only via short-range contact interaction but also via an anisotropic, long-range dipolar-dipolar interaction. This leads to a variety of exotic phenomena occurring in them.
At the 5th Physical Institute at the University of Stuttgart, the first BEC of a dipolar quantum gas consisting of Chromium atoms was realized in 2005 [6]. Since then, the atomic species has been changed from Chromium to Dysprosium, which has a magnetic moment of $\mu = 9.93\mu_\mathrm{B}$ with Bohr's magneton μ_B. This is the highest magnetic moment of all stable elements. In this setup, self-bound quantum droplets [7, 8, 9] and supersolid crystals formed from quantum droplets have been observed [10]. At the moment the experiment is being updated to produce larger BECs. Additionally, a quantum gas microscope is being implemented. This will allow single-site resolving of atoms trapped in an optical potential and the study of Fermi- and Bose-Hubbard models [11, 12].
In this thesis an absorption imaging system is set up and the effects of imaging at high intensities are studied. In experiments with ultracold atoms, it is necessary to perform imaging in order to gain information about the size, position, and density of the trapped atom cloud. One of the most used imaging methods is absorption imaging, as it is versatile and robust. Using Beer's law is a simple way to calculate the atom densities from these images. Only few calibrations are necessary to get to an estimate for the atom number. This estimation can however deviate drastically from the real atom number, depending on the imaging conditions: The higher the intensity of the imaging beam, the larger this deviation will be as the atomic transition saturates. In these cases, Beer's law can be modified to include this saturation effect. For this precise atom reconstruction, several calibration measurements are necessary.
A short overview of the theory of optical imaging is given in Chapter 2. The interaction of a two-level system with light is described, utilizing a semiclassical approach, and the modified Lambert-Beer law is discussed (Chapter 3). In preparation for the absorption imaging, two CCD cameras used in the experiment are characterized. For

the quantum gas microscope, the use of an EMCCD camera is necessary, as it can be used to detect small numbers, up to only one, of photons. These characterizations are described in Chapter 4. Afterwards, the optical setup is designed, simulated and characterized (Chapter 5). The results of using wavelengths of 421 nm and 626 nm for absorption imaging on Dysprosium are presented in Chapter 6. At last an overview of the necessary steps for setting up an absorption imaging system is given in Chapter 7, so that further imaging setups can be added to the experiment in the future.

2 Theory of optical imaging

As one of the central aims of this thesis is to build and characterize an optical setup for taking absorption images of a cloud of Dysprosium atoms first the necessary theoretical foundation of optical imaging is presented.

2.1 Geometric optics

In geometric optics, light is treated as rays, rather than waves. Effects like diffraction or interference are therefore neglected within this framework. In general, geometric optics is applicable if the diameter of the beam is significantly larger than the wavelength λ. In this case, light beams propagate in straight lines through homogeneous media and are reflected or refracted at surfaces. One of the goals of this thesis is to perform imaging, meaning that light originating from a source is focused on a second point. To achieve this lenses will be used.
Lenses are optical components consisting of a (for the used wavelength) transparent material separated from a surrounding medium, within this thesis air, by polished surfaces. They can focus or disperse light, depending on their specific form. In general, the light beam is refracted twice when passing through a lens: Once when entering the lens and once when exiting. A collimated beam, meaning that all the rays in the beam are parallel, passing through a lens will be focussed after the focal length f. The situation can be simplified if the distance between the surfaces of the lens is small compared to the focal length, this case is called the thin lens approximation. Then the imaging equation of thin lenses [13]

$$\frac{1}{a} + \frac{1}{b} = \frac{1}{f} \tag{2.1.1}$$

is valid. Here a is the distance from the light source to the lens and b is the distance from the lens to the image. From this equation, the behaviour of a two-lens system can be discussed. A collimated beam of light entering this system, as shown in figure 2.1.1, will be focussed after the focal length f_1 of the first lens as can be found from

$$\frac{1}{f_1} = \frac{1}{b} \tag{2.1.2}$$

with $a \to \infty$. This point can then be viewed as a point source. If a second lens is placed one focal length f_2 away from the focus of the first lens the beam will again be

collimated after passing through the first lens. This is called a 4f imaging setup, as shown in Figure 2.1.1, and it has a magnification of [13]

$$M = \frac{f_2}{f_1}. \tag{2.1.3}$$

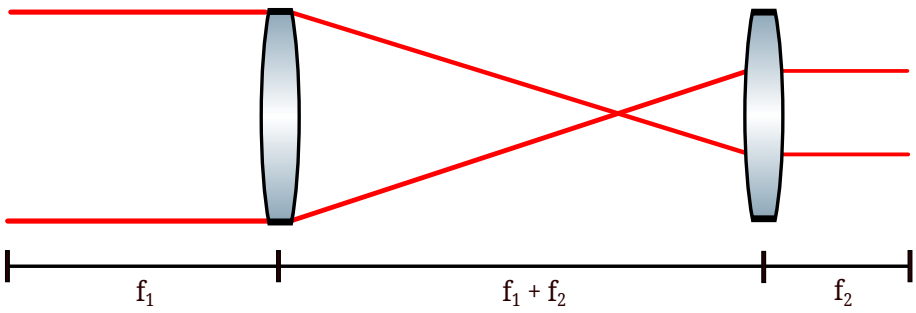

Figure 2.1.1: Two lenses in a 4f imaging setup. Collimated light coming in from the left side gets focused after the focal length f_1. At a distance of f_2 from the focus the second lens is placed, therefore the outgoing beam is again collimated and magnified by a factor of $M = \frac{f_2}{f_1}$.

Combining two 4f setups leads to the situation shown in Figure 2.1.2. With this setup, it is possible to create a flexible imaging system which can be switched between two different magnifications. It has the key feature that only the positions of the two outer lenses relative to each other and the two inner lenses respectively are important for the magnification. Both of these lens pairs fulfil the conditions for a 4f setup. The magnification of the complete system is

$$M = \frac{f_4}{f_1} \cdot \frac{f_2}{f_3} = \frac{M_{14}}{M_{23}} \tag{2.1.4}$$

with the lenses numbered from left to right concerning Figure 2.1.2. The latter magnifications M_{14} and M_{23} are the magnifications of only the outer, respectively inner, lenses. From these considerations one finds that the two inner lenses can be removed, creating again a focused imaging system with magnification M_{14}.

2.2 Airy pattern

If light is diffracted at a circular aperture an Airy pattern can be observed in the image plane. It consists of a central bright spot with concentric bright rings around it. As given in [14] the mathematical expression of this pattern can be derived using the Fraunhofer diffraction integral

$$U(P) = C \int\int_{\mathcal{A}} \mathrm{e}^{-ik(p\xi+q\eta)}\, d\xi d\eta. \tag{2.2.1}$$

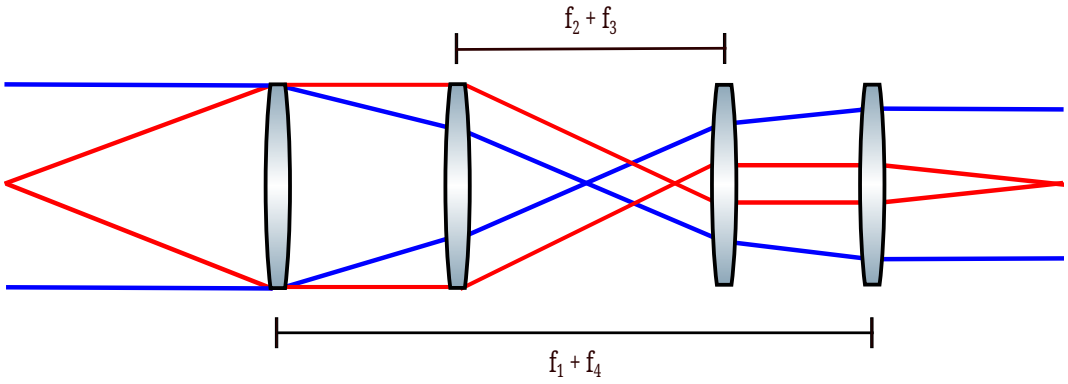

Figure 2.1.2: Four lenses combined from an outer and inner 4f imaging setup. The position of the inner two lenses with respect to the outer two lenses is irrelevant, only their relative distance is important. The magnification of the system is given by $M = \frac{f_4 \cdot f_2}{f_1 \cdot f_3}$

The light is here not anymore treated as a geometric ray but as a wave. $U(P)$ is the amplitude of the electromagnetic field at a point P in the image plane, $\mathcal{A}$ is the area of the aperture, (ξ, η) a point on the aperture and p and q are the direction cosines. The constant C follows from the incoming intensity and conservation of energy.
In the case of a circular aperture, it is convenient to switch to polar coordinates by

$$\rho \cos\theta = \xi \quad \text{and} \quad \rho \sin\theta = \eta \tag{2.2.2}$$

for the aperture as well as

$$w \cos\psi = p \quad \text{and} \quad w \sin\psi = q \tag{2.2.3}$$

for a point in the Airy pattern. Let a be the radius of the aperture. Then the diffraction integral becomes

$$U(P) = C \int_0^{\mathrm{a}} \int_0^{2\pi} \mathrm{e}^{-ik\rho w \cos\theta - \psi} \rho \; d\rho \; d\theta \tag{2.2.4}$$

$$= 2\pi C \int_0^{\mathrm{a}} J_0(k\rho w) \rho \; d\rho. \tag{2.2.5}$$

In order to reduce the expression from the first to the second line the integral definition of the Bessel functions $J_n(x)$ has been used. This integral can be solved analytically leading to the field distribution

$$U(P) = C\pi a^2 \frac{2J_1(kaw)}{kaw}. \tag{2.2.6}$$

The intensity distribution is then given by the absolute square of $U(P)$ and is shown in figure 2.2.1. Due to diffraction, the image is considerably larger then what would be expected by treating the situation purely geometrical, as indicated by the orange line.

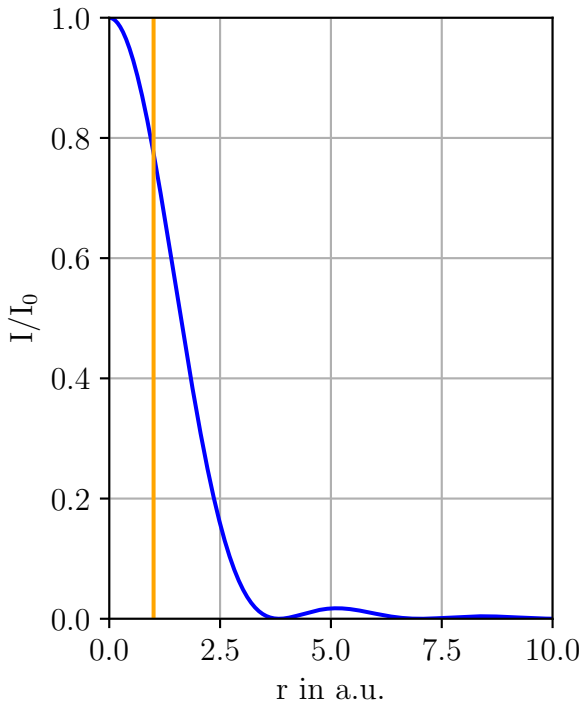

Figure 2.2.1: Normalized intensity distribution $|U(P)|^2$ obtained from the Fraunhofer diffraction integral (2.2.1) for a circular aperture. The orange line indicates the radius of the aperture. If diffraction is not taken into account, the intensity distribution for radii larger than this line would be zero.

2.3 Resolving power and diffraction limit

Using the Airy pattern derived in the previous chapter a quantitative definition for the resolving power of an optical system can be given. The resolving power describes the ability of an optical system to differentiate objects close together from each other. According to the Rayleigh criterion, the minimum distance, where two objects can be separated from each other. The minimum distance where two objects can be separated from each other, according to the Rayleigh criterion, is reached when the maximum of the intensity distribution of one object falls together with the minimum of the other object. The relative positions of the extrema can be found from equation (2.2.6) leading to [14]

$$Y \approx 0.61 \frac{\lambda}{NA} \tag{2.3.1}$$

for the minimal distance Y between two point sources so that their images are distinguishable. If the resolution of a system equals the minimal resolution given by the Rayleigh criterion, the system is called *diffraction-limited*. The numerical aperture

$$NA = n \sin \theta \tag{2.3.2}$$

introduced in the Rayleigh criterion is an important quantity when characterizing imaging systems. It is a measure of the amount of light emitted from a point source in the object plane that can enter the system. n is the refractive index of the medium in which the lens is working, within the scope of this thesis $n = 1$ as all experiments are being done in air. The angle θ is the maximum half angle of a cone of light entering the imaging system. In many cases, it is fixed by the diameter of the objective lens and its focal length.

2.4 Aberrations

The description in the two previous chapters only hold for idealized lenses. In reality deviations from the described properties will occur, so-called aberrations. Aberrations will cause blur or distortions in the generated image, therefore they should be minimized. Chromatic aberrations occur because the diffraction index n is frequency dependent. Monochromatic aberrations in contrast also occur for nearly monochromatic light. In absorption imaging nearly monochromatic light is used, therefore the following description of aberrations will focus on monochromatic aberrations. [13, 15] For near-axis beams Snell's law $\sin\Theta_1 n_1 = \sin\Theta_2 n_2$ can be approximated using $\sin x = x$. The sinus can however also be expanded including higher terms:

$$\sin x = x - \frac{x^3}{3!} + \frac{x^5}{5!} - \mathcal{O}(x^7). \tag{2.4.1}$$

Therefore deviations from the approximated Snell law caused by the first non-linear term are called third-order aberrations. They have been first described by Ludwig von Seidel and are also named Seidel aberrations. The aberrations caused by third-order effects can be given as [16]

$$W(r,\phi,h) = \frac{1}{8}S_I r^4 + \frac{1}{2}S_{II} h r^3 \cos\phi + \frac{1}{2}S_{III} h^2 r^2 \cos\phi^2 + \frac{1}{4}(S_{III} + S_{IV}) h^2 r^2 + \frac{1}{2}S_V h^3 r \cos\phi \tag{2.4.2}$$

with the azimuth angle ϕ, the pupil coordinate r and the object coordinate h. The five coefficients S_i are called the Seidel coefficients and each corresponds to one of the five Seidel aberrations as given in Table 2.4.1. For an ideal imaging system, all five coefficients would equal zero. Now a brief summary of the effects of the five Seidel aberrations is given as described in [13, 17].

Spherical aberration

Spherical aberrations are described by the first term of Equation (2.4.2). They are caused by the dependency of the focal length on the distance of the ray from the optical axis, rays nearer to the optical axis have a larger focal length. Therefore they are particularly important when working with rays with large diameters. If spherical

aberration occurs, the spot size is increased and thus the resolution is decreased.

Coma

Coma occurs either when the object is not on the optical axis or the lens is tilted with respect to the direction of the beam. In these cases, the magnification for rays far from the optical axis is different from near-axis rays. If the image points are also off-axis the image will be distorted to a shape similar to a comet tail, therefore the name.

Astigmatism

Optical systems display astigmatism if the focus positions are different for rays in two perpendicular planes. The image in the image plane, therefore, looks elliptical, not round. If one moves the position of the image plane on the optical axis from one of the foci to the other one the main axis of the ellipse varies and the direction of the long axis is rotated by 90°.

Petzval field

Petzval field curvature occurs at points on the image plane which are so far away from the optical axis that the paraxial approximation is no longer valid. The image can then not be focussed on a plane but on a parabolic surface.

Distortion

The last aberration, the distortion, is again caused by the dependence of the focal length, and therefore the magnification, on the position of the lens. If none of the other four aberrations occurs the image can be completely in focus. However, the position of a point in the image can be moved depending on its distance from the optical axis. Straight lines, for example, then become curved, and lengths and angles are not imaged to scale.

Aberration	**Seidel coefficient**
Spherical aberration	S_I
Coma	S_{II}
Astigmatism	S_{III}
Petzval field	S_{IV}
Distortion	S_V

Table 2.4.1: Connection between the Seidel coefficients used in Equation (2.4.2) and the five aberrations of third order. Adapted from [16].

2.5 Point-spread-function

The intensity distribution of a focused optical system caused by a point source is given by the point-spread function (PSF). If the theoretical PSF is known it can be used to optimize the performance of the real optical system.

The intensity distribution in the image plane $I(x, y)$ can be expressed as

$$I(x, y) = PSF(x, y) *^{2D} O(x, y) \tag{2.5.1}$$

with the two dimensional convolution denoted as $*^{2D}$, the point-spread function $PSF(x, y)$ and the intensity distribution in the object plane $O(x, y)$. One sees immediately that for an object described by a delta distribution $\delta(x, y)$ the PSF equals the intensity distribution in the image plane $I(x, y)$.[18]
The mathematical description of the PSF can be highly complex, especially if aberrations like coma are present, which break the radial symmetry of the PSF. Often times it is, however, sufficient to approximate it with a Gaussian function

$$f(r) = I_0 \exp\left(-\frac{(r - r_0)^2}{w^2}\right). \tag{2.5.2}$$

where w is the width, r_0 the center of the spot, I_0 the maximum intensity and r the radial distance from the center. In the experimental characterisation circular apertures of different sizes will be used to characterise a setup. Therefore the expected intensity profile can be calculated to be

$$I_{\text{ap}}(r) = PSF(r) * \text{rect}\left(\frac{r}{a}\right) \tag{2.5.3}$$

$$= \frac{1}{2} I_0 \sqrt{\pi} w \left(\text{Erf}\left(\frac{a - x}{w}\right) + \text{Erf}\left(\frac{a + x}{w}\right)\right), \tag{2.5.4}$$

where the angular symmetry of the complete imaging system has been used to reduce the problem to one dimension. Here the rectangular function

$$\text{rect}\left(\frac{r}{a}\right) = \begin{cases} 0 & \text{if } |r| > \frac{a}{2} \\ 1 & \text{if } |r| \leq \frac{a}{2} \end{cases} \tag{2.5.5}$$

with the diameter a of the circular aperture is used. By fitting equation (2.5.4) to the measured intensity profile information about the width of the PSF, and therefore the resolution of the system, can be recovered. Note that some deviations from Equation (2.5.4) are to be expected as effects like the Airy pattern are neglected when approximating the PSF with a Gaussian distribution.

3 Atom-light interaction

As the goal of this thesis is to accurately reconstruct the atom number in a cloud of Dysprosium atoms, the interaction between these atoms and the imaging light has to be described first, especially focusing on absorption. For this, a semiclassical approach is chosen, in which the electromagnetic field is not quantized, but the atoms are.

3.1 The two-level atom

The energy structure of an atom can be highly complicated with a multitude of states and possible transitions. Transitions used for absorption imaging are chosen so that they can be well approximated as a two-level system. For this case, the Hamilton operator can be, as described in [19], given as

$$H_0 = E_\mathrm{g} \left|\mathrm{g}\right\rangle \left\langle\mathrm{g}\right| + E_\mathrm{e} \left|\mathrm{e}\right\rangle \left\langle\mathrm{e}\right| \tag{3.1.1}$$

where $|g\rangle$ and $|e\rangle$ denote the wavefunction of the ground and the excited state and E_g and E_e are the respective eigenenergies of these eigenstates of the unperturbed Hamiltonian. The resonance frequency

$$\omega_0 = \frac{E_\mathrm{e} - E_\mathrm{g}}{\hbar} \tag{3.1.2}$$

with the reduced Planck constant $\hbar$ follows directly from these eigenenergies.
Applying an electric field with amplitude $\mathbf{E}_0$ and a frequency of ω introduces an additional Hamilton operator

$$H_1 = e\mathbf{r} \cdot \mathbf{E}_0 \cos\left(\omega t\right) \tag{3.1.3}$$

perturbing the system. H_1 describes the energy of an electric dipole $-e\mathbf{r}$ interacting with an electric field. As a simplification the dipole moment of the atoms is here only caused by one electron, a more precise treatment would include a sum over all electrons and their respective positions. The new complete Hamilton operator is given by

$$H = H_0 + H_1. \tag{3.1.4}$$

Therefore $|\mathrm{g}\rangle$ and $|\mathrm{e}\rangle$ are no longer eigenstates to this system. It is however possible to write the wavefunction of the perturbed system in terms of the eigenstates of the unperturbed system as

$$\psi(\mathbf{r},t) = c_g(t)\,|\mathrm{g}\rangle\,\mathrm{e}^{-i\omega_g t} + c_e(t)\,|\mathrm{e}\rangle\,\mathrm{e}^{-i\omega_e t}. \tag{3.1.5}$$

Here $\omega_\mathrm{i} = E_\mathrm{i}/\hbar$ has been used as an abbreviation. The time-dependent coefficients are subject to the normalization condition

$$|c_\mathrm{g}|^2 + |c_\mathrm{e}|^2 = 1 \tag{3.1.6}$$

and are the populations of the ground and the excited state. Using these coefficients the density matrix

$$|\psi\rangle\,\langle\psi| = \begin{pmatrix} |c_\mathrm{g}|^2 & c_\mathrm{g}c_\mathrm{e}^* \\ c_\mathrm{g}^* c_\mathrm{e} & |c_\mathrm{e}|^2 \end{pmatrix} = \begin{pmatrix} \rho_{11} & \rho_{12} \\ \rho_{21} & \rho_{22} \end{pmatrix} \tag{3.1.7}$$

can be given, describing not only the populations $|c_\mathrm{g}|^2 = \rho_{11}$ and $|c_\mathrm{e}|^2 = \rho_{22}$ but also the so called coherences ρ_{12} and ρ_{21}. These coherences describe the interaction of the system with the perturbing electric field.
The time evolution of the wavefunction (3.1.5) can be studied by using the time-dependent Schrödinger equation

$$i\hbar\frac{\partial\psi}{\partial t} = H\psi. \tag{3.1.8}$$

Plugging the wavefunction (3.1.5) into the Schrödinger equation leads to a system of coupled differential equation

$$i\dot{c}_\mathrm{g} = \Omega\cos(\omega t)\mathrm{e}^{-i\omega_0 t}c_\mathrm{e} \tag{3.1.9}$$

$$i\dot{c}_\mathrm{e} = \Omega^*\cos(\omega t)\mathrm{e}^{i\omega_0 t}c_\mathrm{g} \tag{3.1.10}$$

with the Rabi frequency

$$\Omega = \frac{\langle\mathrm{g}|e\mathbf{r}\cdot\mathbf{E}_0|\mathrm{e}\rangle}{\hbar} \tag{3.1.11}$$

$$= \frac{e\,\langle\mathrm{g}|x|\mathrm{e}\rangle\,|\mathbf{E}_0|}{\hbar}. \tag{3.1.12}$$

For the second equality, it was assumed that the light is linearly polarized in the x direction, meaning that

$$\mathbf{E} = \mathbf{E}_0\mathbf{e}_\mathrm{x}\cos(\omega t). \tag{3.1.13}$$

Additionally, the dipolar approximation has been used, assuming that the electric field is nearly constant over the length of the atom. Therefore $\mathbf{E}_0$ can be treated as constant and pulled out of the integral in Equation (3.1.11).

3.2 Optical Bloch equations

Now a shortened derivation of the optical Bloch equations can be given. First, the expectation value of the x component of the dipole moment of an atom can be calculated to be

$$D(t)_{\mathrm{x}} = \frac{1}{e}\int \psi^{\dagger}(t) ex \psi(t)\, d^3\mathbf{r} \tag{3.2.1}$$

$$= c_{\mathrm{g}} c_{\mathrm{e}}^2 \langle \mathrm{e}|x|\mathrm{g}\rangle \tag{3.2.2}$$

With the detuning

$$\delta = \omega - \omega_0 \tag{3.2.3}$$

between the resonance frequency ω_0 and the frequency ω of the driving electric field, a new set of variables can be defined according to

$$\tilde{c}_{\mathrm{g}} = c_{\mathrm{g}} \mathrm{e}^{-i\delta t/2} \tilde{c}_{\mathrm{e}} = c_{\mathrm{e}} \mathrm{e}^{i\delta t/2} \tag{3.2.4}$$

which does not affect the populations, so that $\tilde{\rho}_{\mathrm{ii}} = \rho_{\mathrm{ii}}$. With this transformation, the dipole moment can be rewritten as

$$D(t)_{\mathrm{x}} = \langle \mathrm{g}|x|\mathrm{e}\rangle \left(\tilde{\rho}_{12}\mathrm{e}^{i\omega t} + \tilde{\rho}_{21}\mathrm{e}^{-i\omega t}\right) \tag{3.2.5}$$

$$= \langle \mathrm{g}|x|\mathrm{e}\rangle \left(u\cos(\omega t) - v\sin(\omega t)\right). \tag{3.2.6}$$

with

$$u = \tilde{\rho}_{12} + \tilde{\rho}_{21} = \rho_{12}\mathrm{e}^{-i\delta t} + \rho_{21}\mathrm{e}^{i\delta t} \tag{3.2.7}$$

$$v = -i(\tilde{\rho}_{12} - \tilde{\rho}_{21}). \tag{3.2.8}$$

By using Equation (3.1.10) a set of coupled differential equations

$$\dot{u} = \delta v \tag{3.2.9}$$

$$\dot{v} = -\delta u + \Omega(\rho_{11} - \rho_{22}) \tag{3.2.10}$$

$$\dot{w} = -\Omega v \tag{3.2.11}$$

can be found with

$$w = \rho_{11} - \rho_{22}. \tag{3.2.12}$$

These equations fail to describe the exponential decay of the population of the excited state into the ground state if no external field acts on the system. Therefore a damping term has to be added, assuming that the decay is exponential. With this term, one arrives at the optical Bloch equations

$$\dot{u} = \delta v - \frac{\Gamma}{2}u \tag{3.2.13}$$

$$\dot{v} = -\delta u + \Omega(\rho_{11} - \rho_{22}) - \frac{\Gamma}{2}v \tag{3.2.14}$$

$$\dot{w} = -\Omega v - \Gamma(w - 1) \tag{3.2.15}$$

with the natural linewidth Γ. For $t \gg \Gamma^{-1}$ the systems reaches an equilibrium described by the steady state solution

$$\begin{pmatrix} u \\ v \\ w \end{pmatrix} = \frac{1}{\delta^2 + \Omega^2/2 + \Gamma^2/4} \begin{pmatrix} \Omega\delta \\ \Omega\Gamma/2 \\ \delta^2 + \Gamma^2/4 \end{pmatrix}. \tag{3.2.16}$$

From this solution, the population of the excited state can be found to be

$$\rho_{22} = \frac{\Omega^2/4}{\delta^2 + \Omega^2/2 + \Gamma^2/4}. \tag{3.2.17}$$

3.3 Light absorption

From this treatment of the two-level atom, the necessary theory for absorption imaging can be developed. In the limit of low intensities absorption can be described by Beer's Law

$$\frac{dI}{dz} = -\kappa(\omega)I = -N\sigma(\omega)I \tag{3.3.1}$$

where the absorption coefficient $\kappa(\omega)$, the atom density N and the scattering cross section $\sigma(\omega)$ have been introduced. Additonally the optical density can be defined as $od = N\sigma(\omega)$ This equation states that the attenuation $\frac{dI}{dz}$ is proportional to the atom density N. It is derived from the intuitive idea, that photons scatter with atoms, depending only on the scattering cross section $\sigma(\omega)$ and the density of photons N. This is however not true for all cases. At high intensity, the atoms reach a limit, and the transition saturates. Equation (3.3.1) is therefore only valid for intensities, where the number of atoms in the ground state N_1 is much larger than the number of atoms in the excited state N_2. If this constraint is released Equation (3.3.1) needs to be modified to

$$\frac{dI}{dz} = -(N_1 - N_2)\sigma(\omega)I. \tag{3.3.2}$$

Within this equation, the effects of absorption as well as stimulated emission are included. Considering this and the conservation of energy, the scattering cross section is found to be

$$\sigma(\omega) = \frac{\rho_{22}\Gamma\hbar\omega}{\omega I} = 3\frac{\pi^2 c^2}{\omega_o^2}\Gamma g_{\mathrm{H}}(\omega) \tag{3.3.3}$$

$$\approx 3\frac{\lambda_0^2}{2\pi} =: \sigma_0. \tag{3.3.4}$$

Here c is the speed of light and

$$g_{\mathrm{H}}(\omega) = \frac{1}{2\pi}\frac{\Gamma}{(\omega - \omega_0)^2 + \Gamma^2/4} \tag{3.3.5}$$

is the line shape function of a Lorentzian profile. For the last approximation, it was assumed that light is absorbed exactly at the resonance frequency ω_0. This will not be true in the experiment and a correction factor for this situation is estimated in Chapter 3.6.
If the intensity of the incoming light is so high that the rate of absorption of photons is larger than the rate of decay from the excited state, the transition will saturate. The saturation intensity is defined as

$$I_{\mathrm{sat}}(\omega) = \frac{\hbar\omega\Gamma}{2\sigma(\omega)} \leq \frac{\pi}{3}\frac{hc\Gamma}{\lambda^3} \tag{3.3.6}$$

where the right expression is the maximum saturation intensity. As this saturation of the transition will reduce the number of absorbed photons Beer's Law has to be modified to [20]

$$\frac{dI}{dz} = -N\sigma(\omega)\frac{I}{1 + I/I_{\mathrm{sat}}}. \tag{3.3.7}$$

The real saturation intensity and absorption cross section will deviate from this theoretical value. Reasons can be imperfections in the polarization of the imaging beam and the orientation of the magnetic field. To compensate for this effect two parameters $\alpha, \beta > 1$ can be defined so that

$$I_{\mathrm{sat}}^{\mathrm{eff}} = \alpha I_{\mathrm{sat}} \quad \text{and} \quad \sigma^{\mathrm{eff}} = \frac{\sigma}{\beta}. \tag{3.3.8}$$

These parameters have to be experimentally calibrated.
Finally, Equation (3.3.7) can be integrated along the z direction to find an explicit expression for the column density

$$N = -\frac{1}{\sigma(\omega)}\left(\ln\left(\frac{I_{\mathrm{out}}}{I_{\mathrm{in}}}\right) + \frac{I_{\mathrm{in}} - I_{\mathrm{out}}}{I_{\mathrm{sat}}}\right), \tag{3.3.9}$$

where I_{out} is the intensity of the imaging light after passing through the atoms. Figure 3.3.1 illustrates the deviations between the atom number calculated using simple Beer's law and the modified Lambert-Beer law. For imaging intensities close to or above the saturation intensity I_{sat} the deviation is, for all optical densities, larger than 20% and therefore definitely significant when performing absorption imaging. As a general trend the deviation decreases for larger optical densities. Here however experimental limitations come into play, as the signal to noise ratio of the camera, used to measure the intensities, limits the minimal intensity which can be used for imaging. Ideally these considerations on optical density and imaging intensity are not necessary, as a well calibrated imaging system can account for these deviations by using the modified Lambert-Beer law.

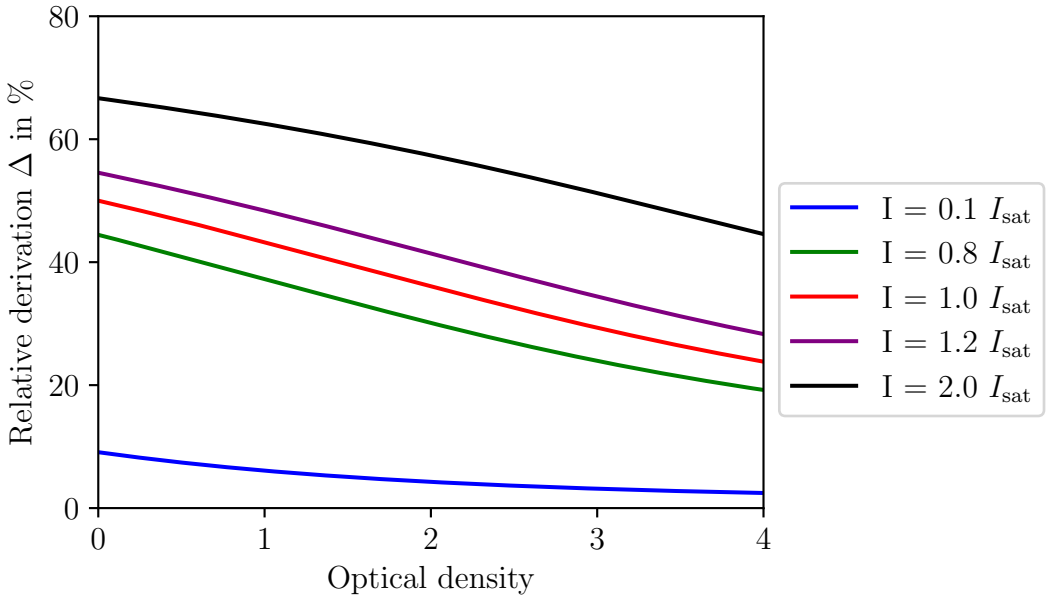

Figure 3.3.1: Relative deviations Δ between Beer's law (3.3.2) and the modified Lambert-Beer law (3.3.9) for different imaging intensities and optical densities. Note that for high optical densities typically higher intensities have to be used in order to get a sufficient signal on the camera, leading to an increase in the deviation from Beer's law.

3.4 Line widths and power broadening

The absorption coefficient $\kappa(\omega)$ depends on the angular frequency ω, therefore it is not only possible to absorb photons directly at the resonance frequency ω_0 but in a wider range. Linewidths have a non-zero width under all circumstances due to natural broadening. If an atom absorbs a photon it gets into an excited state which will exponentially decay back to the ground state. The time constant of this decay is the natural lifetime τ of this state. Then Heisenberg's uncertainty relation can be used to find the uncertainty of the transition frequency: [13]

$$\Delta E \Delta\tau > \hbar \Leftrightarrow \Delta E > \frac{\hbar}{\delta\tau} \Leftrightarrow \Delta\omega > \frac{1}{\tau}. \tag{3.4.1}$$

If only natural broadening is present in the system the last inequality will be an inequality and the natural linewidth can be defined as

$$\Gamma = \tau^{-1}. \tag{3.4.2}$$

Another meachism is power broadening. The absorption coefficient $\kappa(\omega)$ is given as

$$\kappa(\omega) = \frac{N\sigma(\omega)}{1 + I/I_{\text{sat}}(\omega)}. \tag{3.4.3}$$

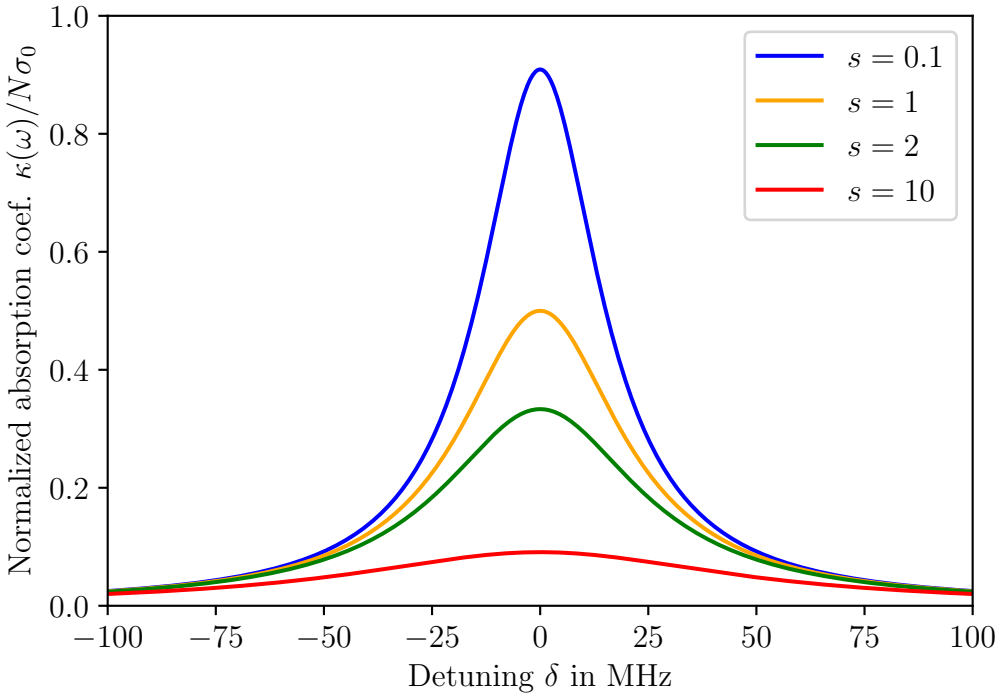

Figure 3.4.1: Normalized absorption coefficient $\kappa(\omega)/N\sigma_0$ against the detuning $\delta = \omega - \omega_0$. For the natural linewidth $\Gamma = 31.9\,\text{MHz}$ is used as this is the wavelenght of the 421 nm transition of Dysprosium used for imaging in the experiment, see Chapter 6 for further details.

In the limit of low intensities, the full width at half maximum (FWHM) can be found from

$$\lim_{I\to 0} \kappa(\omega) = N\sigma(\omega) \tag{3.4.4}$$

to be the same as the FWHM of the scattering cross section, which is the natural linewidth Γ. For higher intensities, the absorption coefficient can be written out to

$$\kappa(\omega) = N\sigma_0 \frac{\Gamma^2/4}{(\omega-\omega_0)^2 + \frac{1}{4}\Gamma^2(1 + I/I_{\text{sat}})} \tag{3.4.5}$$

with a FWHM of

$$\Delta\omega_{\text{FWHM}} = \Gamma\sqrt{1 + \frac{I}{I_{\text{sat}}}}. \tag{3.4.6}$$

Figure 3.4.1 shows absorption coefficients $\kappa(\omega)$ for multiple different saturations s at a natural linewidth of $\Gamma = 31.9\,\text{MHz}$. The increase in FWHM is clearly visible as the absorption coefficient around the resonance decreases.

Equations (3.4.6) and (3.4.5) are only valid in the ideal case. Accounting for experimental imperfections the saturation intensities I_{sat} in both equations needs to be replaced with the effective saturation intensity $I_{\mathrm{sat}}^{\mathrm{eff}}$. By measuring the power broadening and fitting Equation (3.4.6) to the obtained linewidths it is possible to determine this effective saturation intensity.

There can be further broadening mechanism, for example Doppler or transit-time broadening. Within the experiment, however, the atoms are cold enough to neglect these effects. [19]

3.5 Imaging noise

From the treatment in the chapter above two parameters are left that can be chosen in absorption imaging: The exposure time T and the imaging intensity I. In this chapter the relative noise of the atom number is calculated to find the ideal imaging intensity, as discussed in [21].
Experimentally accessible are not the intensities I_{in} and I_{out}, but rather the dimensionless count numbers C_{in} and C_{out} measured by a camera. The photons incident on the camera chip are converted to electrons by the photoelectric effect, the number of electrons is increased and converted to a digital output, the count number C. This number can then be converted into an intensity using the calibrations described in Chapter 4.1.
The count numbers are subjects to a technical noise term Δ_{i} as well as to the shot noise. Shot noise is caused by the discrete nature of the electric charge in the form of electrons. The number of electrons will then fluctuate according to Poisson statistics. The number of photons incident on the sensor is also subject to this shot noise, therefore it might seem reasonable to assume this shot noise directly on the intensities I. This is not justified, however, since the conversion process from photons to photoelectrons by means of the photoelectric effect is again a stochastic process, just like the generation of the photons. If it is assumed that no other noise terms are present and that these two contributions are independent, the variance of the count number can be written as

$$\delta C_{\mathrm{i}}^2 = C_{\mathrm{i}} + \Delta_{\mathrm{i}}. \tag{3.5.1}$$

The variance of the column density can then be calculated directly using Gaussian error propagation to be

$$\delta N^2 = \frac{1}{\sigma^2}\left[\frac{C_{\mathrm{t}} + \Delta_{\mathrm{t}}}{C_{\mathrm{t}}^2}\left(1 + \frac{C_{\mathrm{t}}}{C_{\mathrm{sat}}}\right)^2 + \frac{C_0 + \Delta_0}{C_0^2}\left(1 + \frac{C_0}{C_{\mathrm{sat}}}\right)^2\right]. \tag{3.5.2}$$

The first term describes the noise caused by taking the absorption image itself, and the second one the noise caused by the reference image. The variance could be reduced by increasing the imaging time due to the quadratic terms C_{t}^2 and C_0^2 in the denominators.

This will however on the one hand lead to a larger Doppler shift, which would then have to be compensated by chirping the laser frequency, and on the other hand might lead to saturation of the camera. Effects of interference patterns on the images can also become problematic when using longer exposure times as they might move, increasing the noise on the determined optical densities.

Figure 3.5.1 shows the relative noise for multiple intensities depending on the optical density of the atom cloud. For the sake of shorter notation the saturation parameter $s = I/I_{\mathrm{sat}}$ is introduced here. For low and high densities the relative noise drastically increases. In these regions absorption imaging is not a good choice for probing the atom number. At high densities the noise is increased by the technical limitations of the camera used to detect the intensities, as the intensity coming out of the cloud will be relatively small. For low densities the number of scattered photons is small and it is not possible to calculate the density accurately from this. There is however a large center region with a low relative noise, corresponding to atom densities from roughly 50 to 300 atoms per pixel. Note that these densities are column densities and therefore averaged about the direction of imaging as described with Equation (3.3.9). Within this range, the noise can be minimized by choosing an appropriate imaging intensity. As seen from the figure $I = 0.8I_{\mathrm{sat}}$ minimizes the noise. The densities here are given in units of atoms per pixel. This means that, depending on the magnification of the imaging system, for a given physical density within a cloud the density per pixel can be varied to reduce the relative noise. This leads however to a tradeoff between the resolution and the magnification. If, for example, the number of atoms per pixel needs to be increased to reach the minimum of the relative noise, the size of the image of the cloud on the camera decreases. Therefore less details of the cloud form can be resolved.

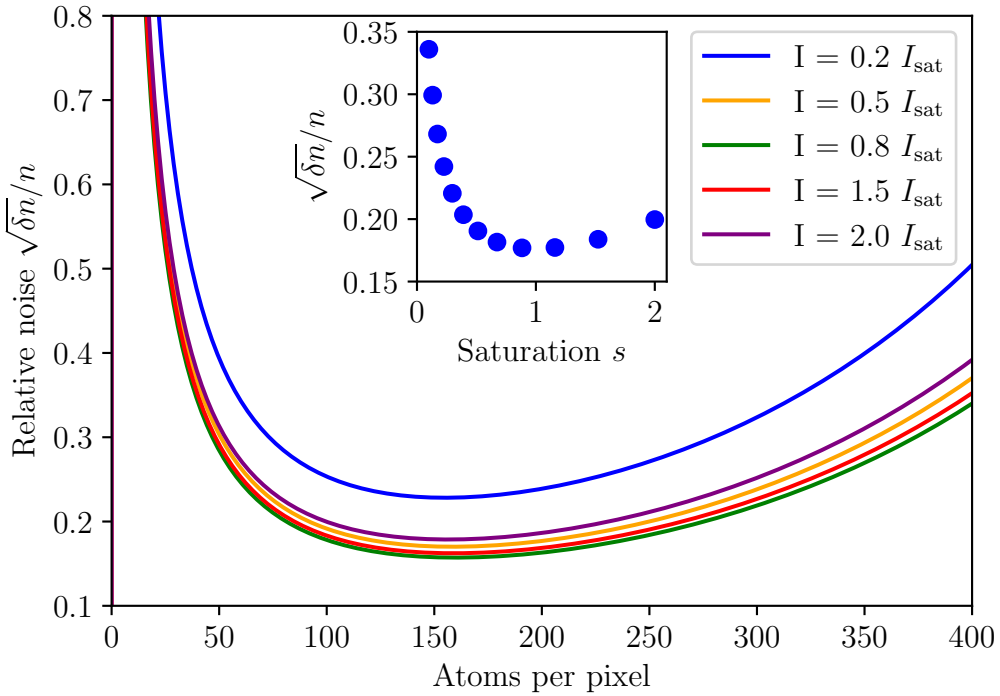

Figure 3.5.1: Relative imaging noise (3.5.2) in dependence of the atom density N per pixel for multiple intensities. At $I = 0.8 I_{\mathrm{sat}}$ the lowest relative noise can be found. The inset shows the relative imaging noise for different saturations s for atom densities of 100 per pixel, a typical value found in the experiment.

3.6 Doppler shift and effective scattering cross section

The dependence of the scattering cross section given by Equation (3.3.3) on the detuning is often neglected when doing absorption imaging. However significant corrections to the reconstructed atom number can arise from this dependence. These are calculated by numerical means here.
The imaged atoms are accelerated by the imaging beam. The force on atoms absorbing photons is given by the momentum transferred per photon multiplied by the scattering rate R_{sc}. Therefore one finds

$$F_{\mathrm{scatt}} = \hbar k \cdot \frac{\Gamma}{2} \frac{s}{1 + s + 4\delta^2/\Gamma^2} \tag{3.6.1}$$

which can then be connected to the velocity of the atoms by the differential equation

$$\frac{dv}{dt} = \frac{F_{\mathrm{scatt}}}{m} \tag{3.6.2}$$

where m is the mass of an atom. This equation is solved numerically to get the velocity profile of the cloud.
If the atoms have a non-zero velocity a Doppler shift occurs. The frequency acting on the atoms is detuned so that

$$\delta = \omega_0 - kv \tag{3.6.3}$$

with the angular frequency ω_0, the wave number k and the speed of the atoms v. It was assumed that the movement of the atoms is parallel to the propagation direction of the beam, in other cases a scalar product between $\vec{k}$ and $\vec{v}$ would need to be used. As the scattering cross section given in Equation (3.3.3) is dependent on the detuning, it will also be dependent on the velocity.
An effective scattering cross section can be defined as the mean cross section over the imaging time T where

$$\sigma_{\text{eff}} = \frac{1}{T} dt \int_0^{\text{T}} \sigma(\omega, \delta). \tag{3.6.4}$$

From this equation the correction factor

$$\gamma = \sigma_{\text{eff}} / \sigma(\omega) \tag{3.6.5}$$

can be introduced. The velocity profile $v(t)$ can be obtained from solving Equation (3.6.2) numerically. With this information Equation (3.6.4) can be integrated numerically, which leads to a correction factor γ dependent on the saturation parameter s as well as the imaging time. Results for selected parameters are shown in Figure 3.6.1. Under some conditions, the correction reaches around 30%. For a high intensity imaging scheme, meaning that $s \approx 1$, this correction is relevant for all imaging times shown in this figure. Note that this correction would also need to be applied to the saturation intensity as given by Equation (3.3.6).

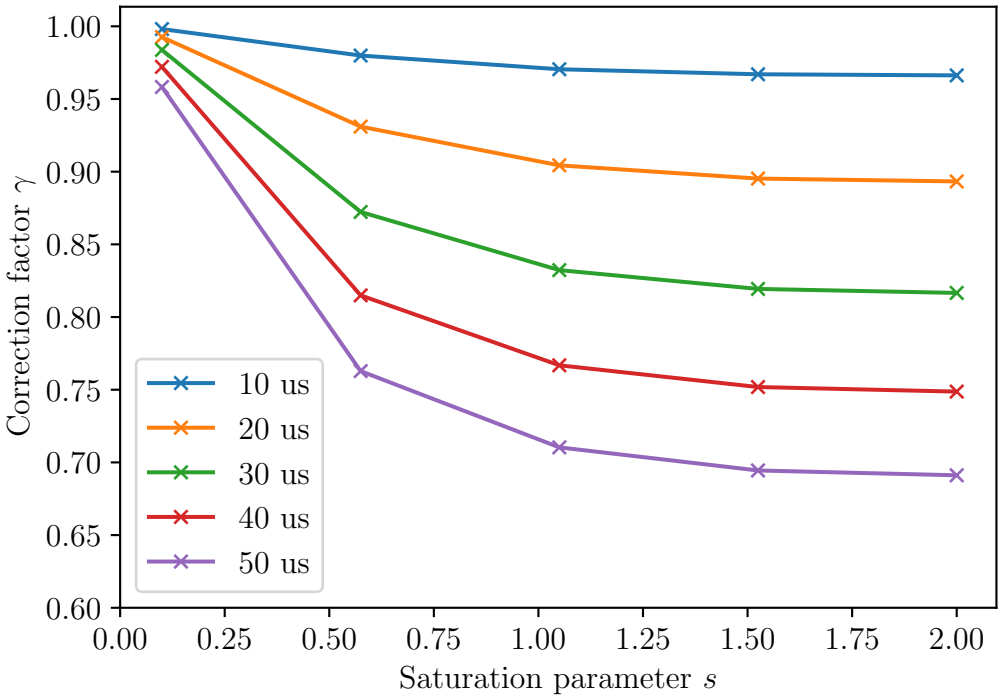

Figure 3.6.1: Correction factors γ caused by the Doppler shift of the atoms depending on the imaging intensity for multiple imaging times t. The parameter is calculated for the transition at 421 nm with a linewidth of $\Gamma = 31.9\,\mathrm{MHz}$. [22] The lines are a guide to the eye.

3.7 Random walk

The atoms are not only accelerated in z-direction, but also perform a random walk in the plane perpendicular to the propagation direction of the imaging beam. This leads to blurring of the image. As discussed in the previous chapter the atoms gain velocity in z-direction due to the photon recoil. However, they also gain a random, isotropic velocity component [4]

$$v_{\mathrm{ran}} = \sqrt{N_{\mathrm{P}}}\frac{h\lambda}{m} \tag{3.7.1}$$

where N_{P} is the number of scattered photons.

The average displacement after a random walk of time t can then be calculated using [23]

$$\Delta r_{\mathrm{ran}} = \int_0^t \sqrt{\langle v_{\mathrm{ran}}^2 \rangle}\, dt' \tag{3.7.2}$$

$$= \int_0^t \sqrt{\frac{2}{3}\frac{h^2\lambda^2}{m^2} R_{\mathrm{sc}}}\, dt' \tag{3.7.3}$$

$$= \frac{2}{3^{3/2}} \frac{h}{m\lambda} t^{3/2} \left(\frac{1}{\Gamma} \frac{1+s}{s} \right)^{-1/2}. \tag{3.7.4}$$

This sets a condition on either the saturation s or the imaging time t, if one wants to take images with good resolution. Figure 3.7.1 shows the maximum imaging time t for the 421 nm and the 626 nm transition of Dysprosium, if the atoms should move not further than one pixel, with a length of 2.4 µm, during the random walk.[1] For the narrow 626 nm the random walk effect is not relevant for any saturation. For the much broader 421 nm transition the situation is different. For high intensities, e.g $s \approx 1$, the maximum imaging time is roughly 40 µs, a value close to the imaging times usually employed in the experiment. However, for determining the atom number the resolution, and therefore the random walk, is not critical and the random walk is not a limiting factor.

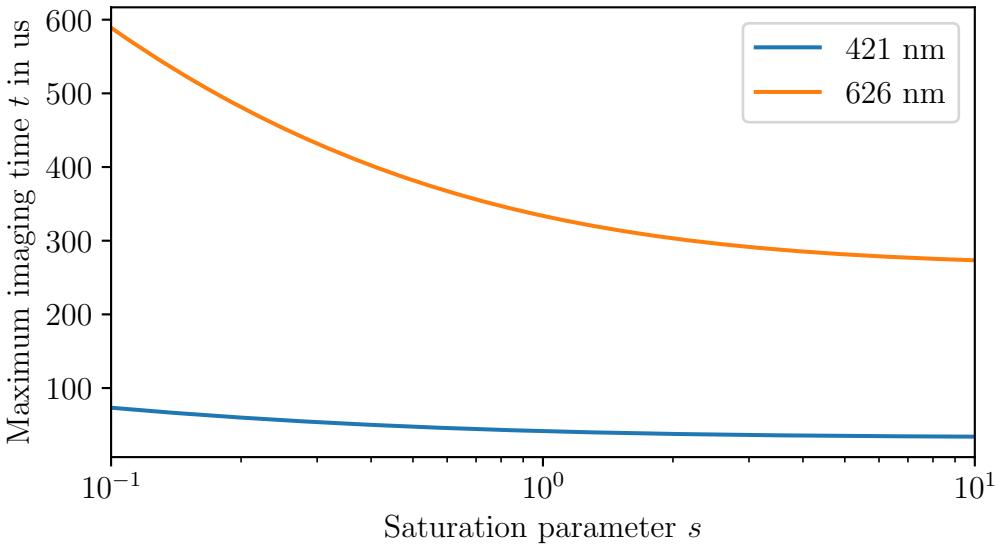

Figure 3.7.1: Maximum imaging times calculated from Equation (3.7.4) for two different transitions of Dysprosium if the atoms are not to move more than 2.4 µm during the imaging.

[1] These requirements are chosen for imaging an atom cloud with a magnification of $M = 1$ and the pixel size of a BFS-U3-63S4M-C CCD camera, which is used in the experiment.

4 Camera characterisation

Within the Dysprosium quantum gas experiment, multiple cameras are used to gather information about the atoms. To calculate intensities from CCD camera images a careful calibration of the gain and the quantum efficiency is necessary. If these are known the measred number of counts can be, using the gain, converted into the number of photoelectrons and, using the quantum efficiency, these can then be converted into the number of photons incident on each pixel of the CCD sensor. By characterizing EMCCD cameras their suitability for single photon detection and, therefore, their use in the quantum gas microscope, can be evaluated. In this chapter, an overview of the necessary theory is given and the results of characterising two types of CCD and two types of EMCCD cameras are given.

4.1 CCD camera characteristics

Charge-coupled device (CCD) cameras are one of the dominating types of cameras not only in scientific but also in general consumer applications. In order to calculate the intensity distribution of an image it is necessary to first calibrate the camera, which will be done in this chapter. First, a brief overview of the working principle of CCD cameras is given, then the experimental results are presented.

4.1.1 Theoretical background

In general CCD sensors consist of a bulk material, a doped semiconductor, and many electrodes placed in an array on top of the bulk material. If a voltage is applied to one of these electrodes a potential well forms beneath it. Photons with an energy larger than the bandgap of the semiconductor used can excite electrons from the conduction into the valence band, generating an electron-hole pair in the semiconductor. Due to the potential well, the minority charge carriers are collected in the well. After the exposure, the charge carriers in the potential well are moved to neighbouring potential wells until the end of the sensor array is reached and they can be read out. The number of electrons is first increased by an on-chip amplifier and, depending on the chosen settings and the camera type, may again be amplified by an off-chip amplifier. The voltage generated by these electrons is then fed into an analogue-to-digital converter, finally leading to a digital signal proportional to the number of photons that reached

the pixel during the exposure time. A more detailed treatment of the physics of CCD cameras can be found in [24].
The generated image is affected by various noise sources as well as the dark current. The dark current is caused by the thermal generation of electrons in the depletion region, the bulk material as well as surface states. As the number of electrons generated is directly proportional to the exposure time this contribution can be simply subtracted from the image. Due to fluctuations of the dark current, this will lead to an increased noise in the image. Note that in general, the dark current is different for different pixels creating the so-called fixed pattern noise. The number of primary photoelectrons (PPE) on the detector is also affected by shot noise. The conversion from photons to PPEs is a stochastic process. Due to the discrete nature of the electric charge, in the form of electrons, it can be described using Poisson statistics, the variance of the number of PPEs then equals the number of PPEs: [25]

$$\delta n_{\mathrm{PPE}}^2 = n_{\mathrm{PPE}}. \tag{4.1.1}$$

Further noise is added to the signal by both amplifiers and the analogue-to-digital converter. These contributions can be summarized into the read-out noise σ_{r}. With these pieces of information a first model describing the measured signal can be constructed. Let N_e be the noise in electrons, consisting of the aforementioned noise sources. Therefore

$$N_{\mathrm{e}}^2 = \sigma_{\mathrm{r}} + n_{\mathrm{e}} \tag{4.1.2}$$

which can be translated into the number of counts measured by

$$N_{\mathrm{C}}^2 = \frac{1}{g}\sigma_{\mathrm{r}} + \frac{1}{g}n_{\mathrm{c}}. \tag{4.1.3}$$

The measured signal has therefore a linear affine relation to the variance of the signal In this equation, the gain g has been introduced. It relates the number of electrons on a pixel to the number of counts on the final image and is given in units of electrons per counts.[26]
After characterising the gain the quantum efficiency

$$QE = \frac{n_{\mathrm{e}}}{n_{\mathrm{ph}}} \tag{4.1.4}$$

as the ratio between generated photoelectrons and incoming photons can be measured. The number of photons can be found by multiplying the photon flux

$$\Phi = \frac{I}{\hbar\omega} \tag{4.1.5}$$

with the exposure time

$$n_{\mathrm{ph}} = \frac{It}{\hbar\omega} = \frac{It\lambda}{hc}. \tag{4.1.6}$$

Here t is the exposure time, λ the wavelength of the used light and c the speed of light.[17]

4.1.2 Characterisation of the BFS-U3-63S4M-C camera

Based on the theory developed in the previous chapter the BFS-U3-63S4M-C camera by FLIR was characterised, relevant documents for this camera are available in [27]. It is a monochrome CMOS camera with a rolling shutter, a summary of its properties is given in Table 4.1.2. To measure the gain the camera is illuminated nearly uniformly using a LED and two diffusers. A region of 100 pixels by 100 pixels with nearly constant intensity is selected from an image and the mean count number as well as its variance are calculated. Figure 4.1.2 shows three histogramms calculated from these images. It can be seen that the distributions are not cut off and have the form of Gaussian distributions, showing that these measurements are valid to determine the gain. The left plot in Figure 4.1.1 shows an exemplary variance-signal plot with a linear fit function according to Equation (4.1.3). The right part shows the gain set in the control software g_s as well as the corresponding measured values g_m. An affine function is fitted to the data from which the equation

$$g_\mathrm{m} = (0.97 \pm 0.02)\,\mathrm{dB} \cdot g_\mathrm{s} + (13.1 \pm 0.3)\,\mathrm{dB} \tag{4.1.7}$$

is found, describing how the real gain g_m is related to the set gain g_s. Especially one finds the on-chip gain to be

$$g = 0.21 \pm 0.01 \frac{\mathrm{e}^-}{\mathrm{ADU}}. \tag{4.1.8}$$

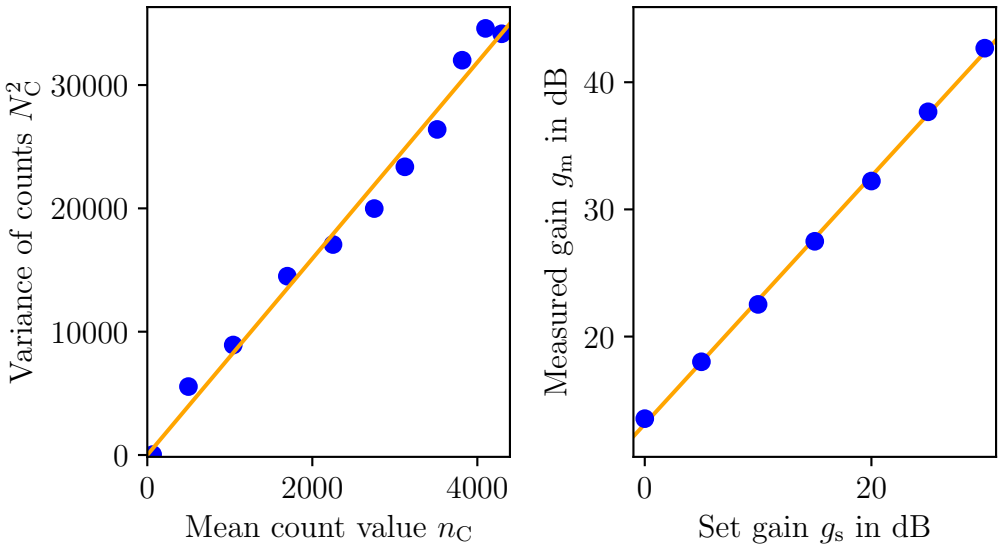

Figure 4.1.1: The left plot shows the variance over the mean signal for a uniformly illuminated image with a fit according to Equation (4.1.3). The right figure shows the measured gain plotted over the set gain, again with a linear fit function.

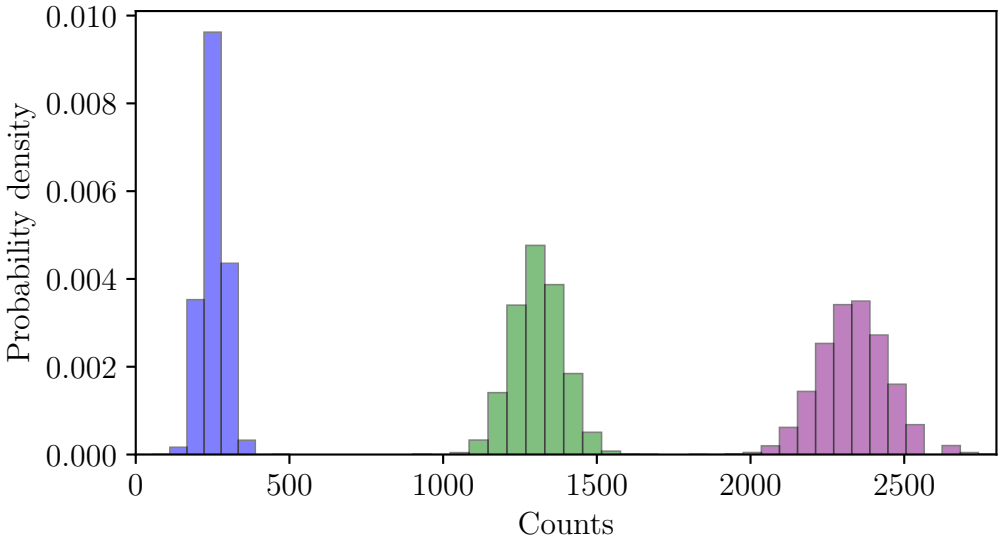

Figure 4.1.2: Histogram of the count distributions for one image with a low, medium and high mean count number. For all three cases the distribution follows a Gaussian distribution, which is fully captured and not cut off. It follows that all data points can be used for determining the gain as shown in Figure 4.1.1, in contrast to what is observed for the second characterized camera discussed in the next section.

The dark current was measured by taking 100 images with exposure times ranging between 1 s and 9 s. The mean count value n_C for all pictures with an equal exposure time is calculated, as shown in Figure 4.1.3 and plotted over the exposure time. By fitting an affine function and multiplying with the gain one finds for the dark current

$$d = 21 \pm 4 \ \frac{\mathrm{e}^-}{\mathrm{s}}. \tag{4.1.9}$$

For the absorption imaging techniques employed in this thesis exposure times of a few ten microseconds are chosen, therefore the dark current is negligible.

The third parameter investigated is the read-out noise. Two dark images with the minimal possible exposure time of 16 µs are taken. They are subtracted from each other to correct for flat-field irregularities and an offset. The variance of the difference image is the read-out noise, which can be converted from counts into electrons using the calibrated gain. For this camera, the read-out noise was found to be

$$\sigma_R = 2.55 \ \mathrm{e}^-. \tag{4.1.10}$$

Lastly to measure the quantum efficiency a beam of blue light with a wavelength of 421 nm is imaged using the camera. The intensity is measured using a handheld power meter and the number of photoelectrons is calculated from the measured count value and the gain. Using a $\frac{\lambda}{2}$ plate and a polarizing beam splitter the intensity is varied. From all measurements the quantum efficiency

$$QE = 0.70 \pm 0.02 \tag{4.1.11}$$

was found. The precision of this measurement is limited by the fluctuation of the intensity of the used beam. It was observed that the measured power fluctuated by around 5% during the measurement, which takes a few seconds as multiple images are taken. This could be resolved by employing a beam splitter, directing one of the beams onto the camera and measuring the power in the second beam simultaneously to taking the images.

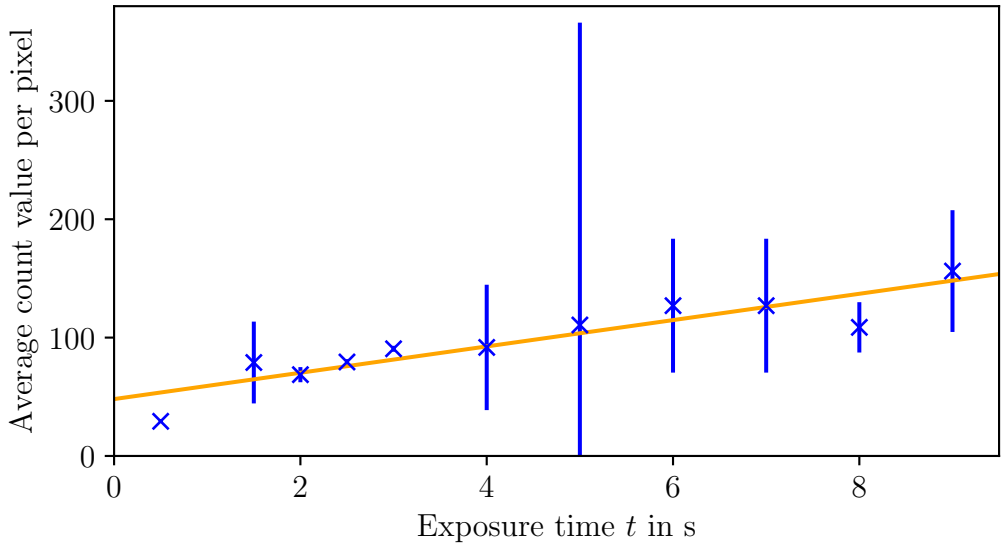

Figure 4.1.3: Average count value per pixel calculated from the mean of 100 dark images each with the shown exposure times. The orange line is a linear affine function, the slope of this function corresponds to the dark current in $\frac{\mathrm{ADU}}{\mathrm{s}}$. The gain was set to 30 dB, using this information the dark current is converted in $\frac{\mathrm{e}^-}{\mathrm{s}}$.

Table 4.1.1: Properties of the BFS-U3-63S4M-C camera. The values in brackets are taken from the datasheet and the imaging performance measurements provided by the manufacturer. [27]

Property	**Value**
Resolution	3072 px x 2048 px
Pixel size	2.4 µm x 2.4 µm
Dynamic range	14 bit
Quantum efficiency at 421 nm	0.70 ± 0.02 (≈ 0.77)
Gain	$0.21 \pm 0.01 \ \frac{e^-}{ADU}$ ($0.23 \ \frac{e^-}{ADU}$)
Read noise	2.55 e^- (2.45 e^-)
Dark current	$21 \pm 4 \ \frac{e^-}{s}$

4.1.3 Characterisation of the BFS-U3-70S7M camera

The BFS-U3-70S7M is again a monochromatic CMOS camera by FLIR, it possesses, however, a global shutter. Relevant documents are available in [28]. For this camera, the same measurements are done as for the one described above. Figure 4.1.4 again shows an exemplary variance-signal plot. The first three data points strongly deviate from the expected linear behaviour and are excluded from further evaluations. The reason for this deviation can be understood from Figure 4.1.5. As the probability distribution in images with low illumination is not Gaussian anymore because it is cut-off, the variance of the distribution calculated using

$$\mathrm{Var}(X) = \mathrm{E}(x^2) - (\mathrm{E}(x))^2 \tag{4.1.12}$$

does not equal the effective variance of the Gaussian distribution of the count values. Here the expectation value of a variable is denoted as E. Omitting these datapoints one can calibrate the gain to

$$g_\mathrm{m} = (0.98 \pm 0.01)\,\mathrm{dB} \cdot g_\mathrm{s} + (9.31 \pm 0.17)\,\mathrm{dB} \tag{4.1.13}$$

with the on-chip gain

$$g = 0.33 \pm 0.01 \frac{\mathrm{e}^-}{\mathrm{ADU}}. \tag{4.1.14}$$

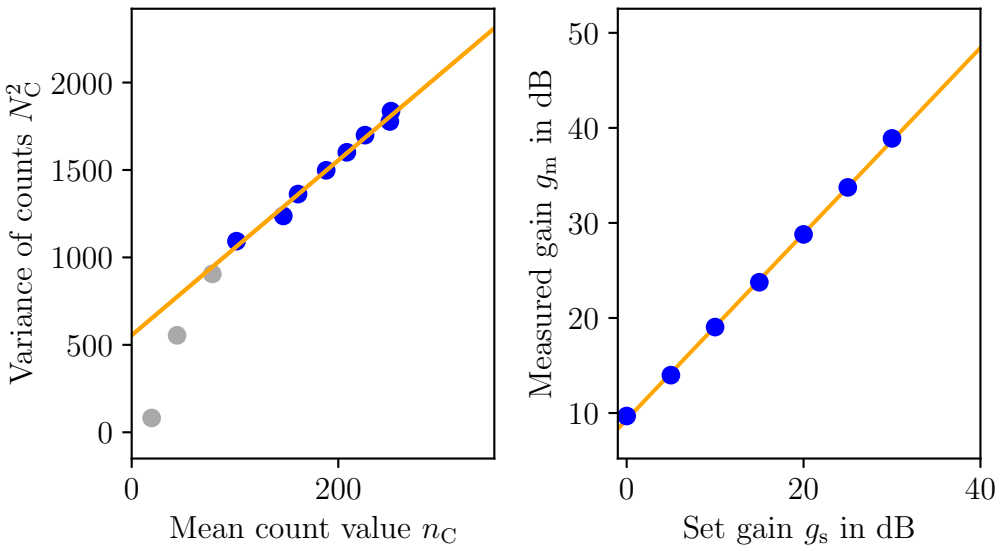

Figure 4.1.4: The left plot shows the variance over the mean signal for a uniformly illuminated image with a fit according to Equation (4.1.3). Points not included in the evaluation are shown in grey. The right figure shows the measured gain plotted over the set gain, again with a linear fit function.

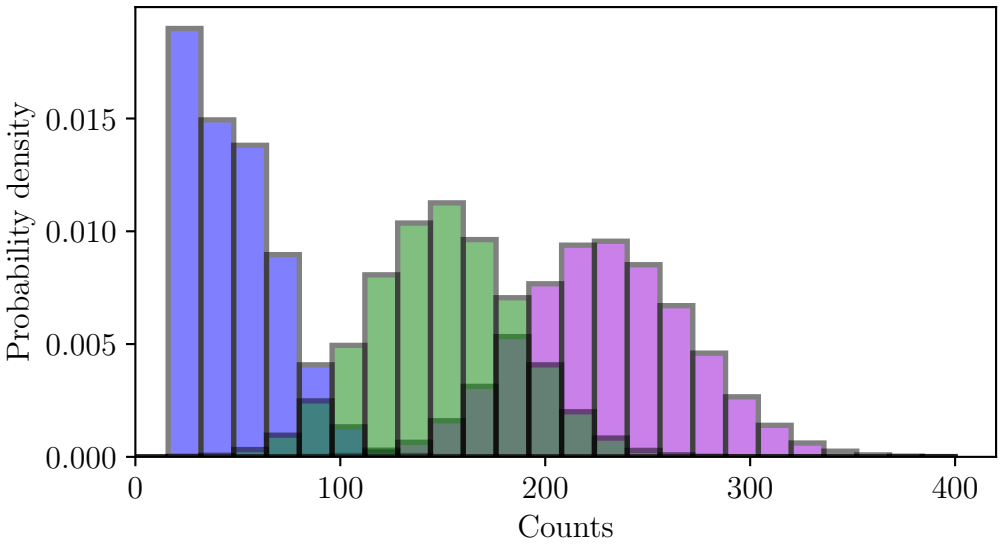

Figure 4.1.5: Histogram of the count distributions for one image with a low, medium and high mean count number. The distribution of the image with low illumination is cut off. Therefore the variance calculated using Equation (4.1.12) underestimates the variance of the count distribution.

Again the read-out noise was determined to be

$$\sigma_{\text{read}} = 3.63\text{e}^- \tag{4.1.15}$$

and the quantum efficiency to be

$$QE = 0.44 \pm 0.02 \tag{4.1.16}$$

The dark current was measured to be

$$d = 62 \pm 7 \ \frac{\text{e}^-}{\text{s}}. \tag{4.1.17}$$

Table 4.1.2: Properties of the BFS-U3-70S7M camera. The values in brackets are taken from the datasheet and the imaging performance measurements provided by the manufacturer. [28]

Property	**Value**
Resolution	3208 px x 2200 px
Pixel size	4.5 µm x 4.5 µm
Dynamic range	12 bit
Quantum efficiency at 421 nm	(0.44 ± 0.02) (≈ 0.56)
Gain	$0.33 \pm 0.01 \frac{\text{e}^-}{\text{ADU}}$ ($0.41 \ \frac{\text{e}^-}{\text{ADU}}$)
Read noise	3.63 e^- (2.70 e^-)
Dark current	$62 \pm 7 \ \frac{\text{e}^-}{\text{s}}$

4.2 EMCCD camera characteristics

As regular CCD cameras have a read-out noise of a few electrons, it is not possible to directly detect single photons with them. Electron multiplying CCD (EMCCD) cameras enable measurements beyond this limit, making it possible to count single photons. This is achieved by amplifying the number of electrons even before the read-out.

4.2.1 Theoretical background

The electron multiplication is being done in a multiplication register. In these registers, spurious charges can occur by impact ionization, for traditional CCD cameras an undesirable side effect. In EMCCD cameras, however, the probability of creating spurious charges is enhanced by using a register with hundreds of cells. Then the strength of the amplification can be controlled by adjusting the clock voltage. Gains of up to 1000 are achievable. [29]

The distribution of the number of secondary photoelectrons (SPE) n_S after the amplification of the primary photoelectrons (PPE) n is given by the Erlang distribution [30]

$$P_\mathrm{n}(n_\mathrm{S}) = \frac{n_\mathrm{S}^{n-1} e^{-n_\mathrm{S}/g}}{g^n \Gamma(n)} \Theta(x). \tag{4.2.1}$$

Here $\Theta(n_\mathrm{S})$ is the Heavyside step function, $\Gamma(n)$ the Gamma function and g the gain described above. This distribution is plotted for multiple values of n in figure 4.2.1. One directly sees a large overlap between the distribution for different numbers of PPEs. With EMCCD cameras it is therefore hard to discriminate exactly the number of PPEs, however, one PPE can be distinguished from the read-out noise, enabling single-photon detection

To characterize an EMCCD camera firstly multiple dark images are taken and from the number of SPEs, a histogram of the probability distribution is calculated. This histogram is defined by the noise sources affecting the camera. Firstly, the read-out noise is modelled by a Gaussian probability distribution $G(n_\mathrm{S})$. Its mean is the offset $n_{\mathrm{S,\ offset}}$ of the picture while its standard deviation is the readout noise σ_read. Secondly, clock-induced charges (CICs) and dark noise generates electrons which are then amplified in the multiplication register. CICs are generated when PPEs are transported from the camera chip into the read-out electronics. This is done by applying a voltage alternating between a low and a high value. Due to this voltage impact ionization can occur within the semiconductor used to build the electronics, generating a free electron. It is not possible to differentiate an electron generated by this mechanism from a PPE. The probability of finding such an electron is p_par. It can be approximated that at most one PPE per pixel is generated by these mechanisms, therefore

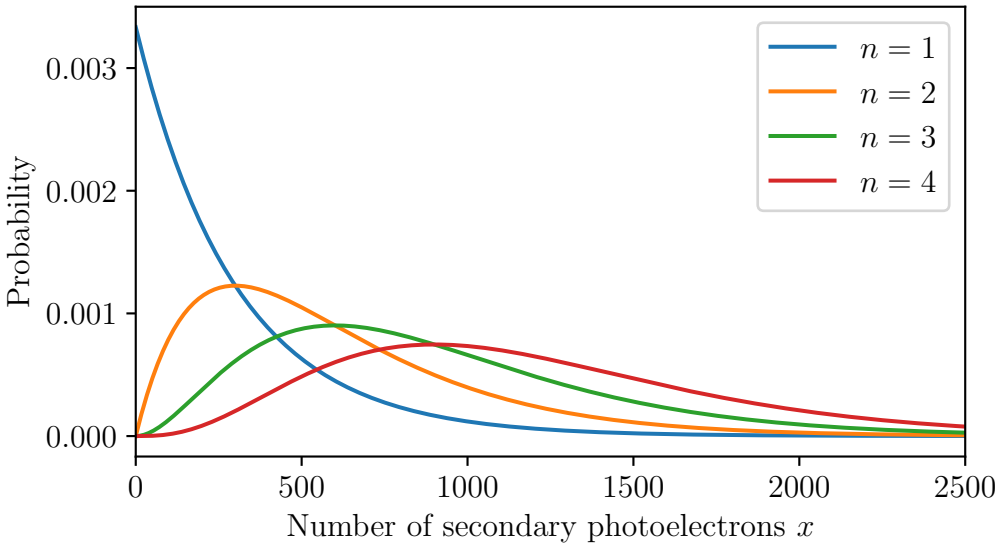

Figure 4.2.1: Plot of the Erlang distribution (4.2.1) for one to four PPEs. From this plot, the limitations of EMCCD cameras can already be seen, as the distributions overlap. Therefore distinguishing exact photon numbers is not easily possible.

the probability of finding $n_{\mathrm{S,\,par}}$ SPEs is given by [31]

$$P_{\mathrm{par}}(n_{\mathrm{S,\,par}}) = p_{\mathrm{par}} P_1(n_{\mathrm{S,\,par}}) = \frac{p_{\mathrm{par}} e^{-n_{\mathrm{S,\,par}}/g}}{g}. \tag{4.2.2}$$

Thirdly, with a probability p_{ser} it is possible that CICs are, by the same mechanism as described for parallel SPEs, generated in the multiplication register. These electrons, called serial CICs, are only amplified by the remaining cells of the register, therefore the probability of finding x_{ser} SPEs is given by [31]

$$P_{\mathrm{ser}}(n_{\mathrm{S,\,ser}}) = \sum_{\mathrm{l}=1}^{\mathrm{m}} \frac{p_{\mathrm{ser}} e^{-n_{\mathrm{S,\,ser}}/p_{\mathrm{c}}^{\mathrm{m\text{-}l}}}}{p_{\mathrm{c}}^{\mathrm{m\text{-}l}}}. \tag{4.2.3}$$

p_{c} is the probability of duplicating an electron at a cell of the multiplication register. The complete distribution is then obtained as the convolution of these three distributions as

$$P_{\mathrm{dark}}(n_{\mathrm{S}}) = G(\sigma_{\mathrm{read}}) * P_{\mathrm{par}} * P_{\mathrm{ser}} \tag{4.2.4}$$

$$\approx G(\sigma_{\mathrm{read}}) * P_{\mathrm{par}} \tag{4.2.5}$$

where the contribution of the serial spurious charges can be neglected, as it is not necessary for the characterisation of the EMCCD camera. In practice, a Gaussian distribution is fitted to the peak in the measured data while the gain is extracted from

the exponentially decaying tail of the distribution as shown in figure 4.2.2. From these fits the gain g and the read-out noise σ_{read} is received. Their ratio g/σ_{read} is the key characteristic of an EMCCD camera as it quantifies how well a single photon event can be distinguished from the read-out noise.
In order to detect a photon a threshold σ_{tres} has to be set. Images are then binarized according to

$$I_{\text{i,j}} = \begin{cases} 1 & n_{\text{i,j}} > \sigma_{\text{tres}} \\ 0 & n_{\text{i,j}} < \sigma_{\text{tres}}. \end{cases} \tag{4.2.6}$$

$n_{\text{i,j}}$ is the number of SPEs in a pixel and $I_{\text{i,j}}$ is the value of the binarized image. Due to the statistical nature of the PPE amplification process not all PPEs are recognized correctly in the binarized images. The probability of identifying a PPE correctly is given by the extraction fidelity

$$P(1 \to 1) = \int_{\sigma_{\text{tres}}}^{\infty} \frac{e^{-x/g}}{g} dx = e^{-\sigma_{\text{tres}}/g} = e^{-k \cdot \sigma_{\text{read}}/g}. \tag{4.2.7}$$

where the exponent has been separated in the ratio of gain and read-out noise as well as a parameter k which relates the read-out noise to the threshold as $\sigma_{\text{tres}} = k \cdot \sigma_{\text{read}}$ The extraction fidelity could be optimized by choosing a smaller threshold. This however increases the probability of incorrectly identifying an event

$$P(0 \to 1) = \int_{\sigma_{\text{tres}}}^{\infty} G(\sigma_{\text{read}}) dx = \frac{1}{2}\left(1 - \text{erf}\left(\frac{\sigma_{\text{tres}}}{\sqrt{2}\sigma_{\text{read}}}\right)\right) \tag{4.2.8}$$

$$= \frac{1}{2}\left(1 - \text{erf}\left(\frac{k}{\sqrt{2}}\right)\right). \tag{4.2.9}$$

Additionally setting a higher threshold will reduce the effect of serial SPEs. For suppressing the read noise using a threshold of around 4 to $5\sigma_{\text{read}}$ would be enough, with serial SPEs high thresholds of up to $8\sigma_{\text{read}}$ need to be used [32]. Therefore a higher ratio of gain and read noise is desirable to optimize the accuracy of detecting single photons.
Two different EMCCD cameras are characterized in this thesis. Their ratio of gain over read noise is measured for different camera settings to find the optimum.

4.2.2 Characterization of the Andor iXon Ultra 888 EMCCD camera

The histograms expected according to Equation (4.2.5) are calculated from 70 images without illumination. There are several possible settings that can be changed:

- **Gain:** The gain setting controls the clock voltage and therefore the probability p_c of generating a second electron in one of the cells of the multiplication register. The maximum value is 1000.
- **Preamp-gain:** The preamplifier gain can be reduced to prevent saturation of the well capacity. For low-light applications, it is strongly suggested to use the highest setting as this will result in the highest sensitivity.[33]
- **Temperature:** The camera can be cooled down to $-70\,^{\circ}\mathrm{C}$ using a multi-stage thermoelectric cooler. Colder temperatures could be achieved by water-cooling the system, this was however not done in this thesis. In terms of camera performance colder temperatures are desirable as they will reduce the dark-current noise.[34]
- **Vertical shift speed:** The vertical shift speed determines how fast the rows of the sensor array are moved into the shift register. The time this shifting takes can be varied from $0.6\,\mu\mathrm{s}$ to $4\,\mu\mathrm{s}$.[1]
- **Horizontal shift speed:** The horizontal shift moves charges from the shift register into the multiplication register. Possible shift rates range from $1\,\mathrm{MHz}$ to $30\,\mathrm{MHz}$.

The best performance was achieved for a horizontal shift rate of $1\,\mathrm{MHz}$, a vertical shift period of $0.60\,\mu\mathrm{s}$ and the lowest possible temperature of $-70\,^{\circ}\mathrm{C}$. These settings resulted in a gain over read-noise ratio of

$$\frac{g}{\sigma_{\mathrm{read}}} = 57.41 \pm 0.60, \tag{4.2.10}$$

the corresponding histogram is shown in figure 4.2.2. This gain over read-noise ratio corresponds to an extraction fidelity of $(86.99 \pm 0.13)\%$. The probability of wrongly identifying an event at a threshold of $8\sigma_{\mathrm{read}}$ is completely negligible as $P(0 \to 1) \approx 6.2 \cdot 10^{-16}$.

[1] The value of $4\,\mu\mathrm{s}$ is acquired by reading out this information from the camera using the control software. In [34] ANDOR provides information about the shift speeds, indicating that this value could be rounded from $4.33\,\mu\mathrm{s}$.

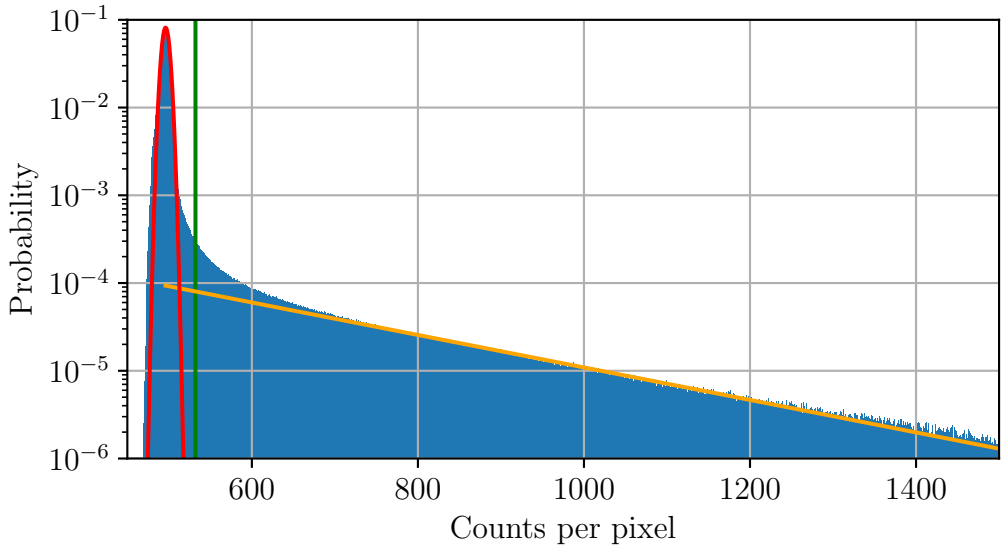

Figure 4.2.2: Histogram calculated from 70 dark images with the described optimal settings. The red line is a Gaussian distribution used to determine the read noise σ_{read}, and the orange line is an exponential decay with the decay constant being the gain g. Serial SPEs, generated in the multiplication register, have a much lower effective gain than SPEs generated before the multiplication register. Therefore they can be found close to the read noise distribution. In this figure, they cause the deviation from the exponential fit shown in orange. The vertical green line is drawn at the threshold of $8\sigma_{\text{read}}$.

Further measurements were done to explore the influence of the mentioned parameters. The results are listed in the Tables 4.2.1, 4.2.2 and 4.2.3. The vertical shift period does not have a large influence on the performance, the horizontal shift rate however does. Setting its values above 10 MHz reduces the achievable gain over read-noise roughly by a factor of 5. Lastly increasing the temperature decreases, as expected, the gain over read-noise significantly.

Table 4.2.1: Gain over read-noise g/σ_{read} for all possible vertical shift periods. The measurements were taken with a horizontal shift rate of 1 MHz and at −70 °C.

Vertical shift period	gain over read-noise	extraction fidelity
4 µs	53.40 ± 1.53	(86.09 ± 0.37) %
2 µs	56.97 ± 0.76	(86.90 ± 0.17) %
1 µs	44.90 ± 1.24	(83.68 ± 0.41) %
0.60 µs	57.41 ± 0.60	(86.99 ± 0.13) %

Table 4.2.2: Gain over read-noise g/σ_{read} for all possible horizontal shift rates. The measurements were taken with a vertical shift period of 4 µs and at −70 °C.

Horizontal shift rate	gain over read-noise	extraction fidelity
1 MHz	53.40 ± 1.53	(86.09 ± 0.37) %
10 MHz	53.11 ± 0.77	(86.02 ± 0.19) %
20 MHz	10.68 ± 0.02	(47.28 ± 0.07) %
30 MHz	9.11 ± 0.01	(41.55 ± 0.04) %

Table 4.2.3: Gain over read-noise g/σ_{read} for multiple different temperatures. The measurements were taken with a vertical shift period of 4 µs and a horizontal shift rate of 1 MHz.

Temperature	gain over read-noise	extraction fidelity
−70 °C	53.40 ± 1.53	(86.09 ± 0.37) %
−60 °C	43.00 ± 0.89	(83.02 ± 0.32) %
−50 °C	44.42 ± 0.20	(83.52 ± 0.07) %
−40 °C	21.91 ± 0.87	(69.41 ± 0.98) %
−30 °C	17.68 ± 0.26	(63.60 ± 0.42) %

4.2.3 Characterization of the Andor iXon 3 EMCCD camera

The Andor iXon 3 EMCCD camera is a precursor to the iXon Ultra series. The camera characterised in this thesis has already been used to study Dysprosium quantum gases, therefore some degradation of the performance is expected.
Figure 4.2.3 shows a histogramm of the dark image for the optimized settings. Here the best result with

$$\frac{g}{\sigma_{\text{r}}} = 18.59 \pm 0.23 \tag{4.2.11}$$

was achieved with similiar parameters as for the iXon Ultra: The temperature was set to −80 °C, the vertical readout speed to the highest value and the horizontal shift rate to the lowest value. Even for the best possible parameters the ratio of gain over read-noise is still too low to perform efficient single photon detection. It might be possible to recalibrate this camera using software provided by Andor Technology, making the camera again suitable for use in the experiment. This has however not been done within this thesis.

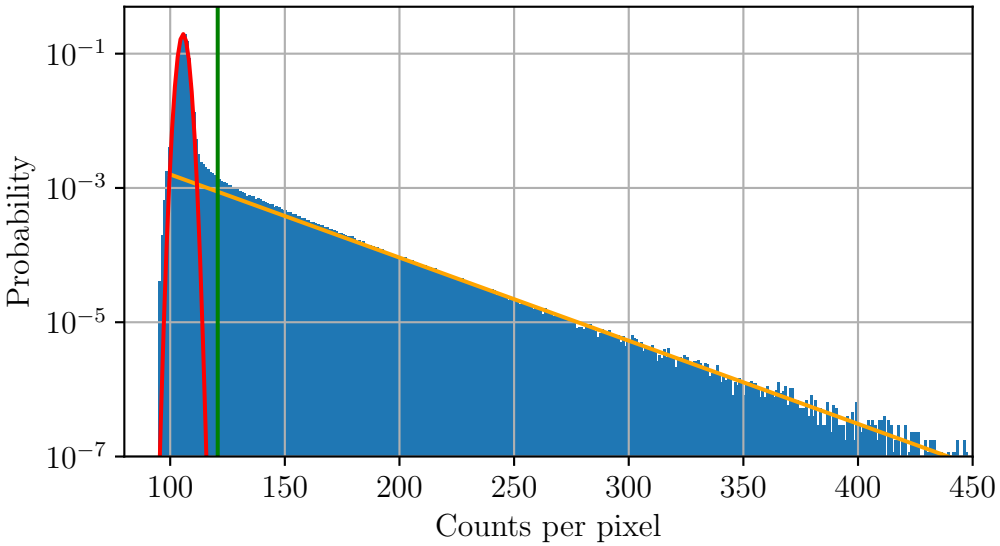

Figure 4.2.3: Histogram calculated from 70 dark images with the described optimal settings. The red line is a Gaussian distribution used to determine the read noise σ_{read}, the orange line is an exponential decay with the decay constant being the gain g. The vertical green line is drawn at the threshold of $8\sigma_{\text{read}}$.

5 Experimental setup

The imaging beam is not directly pointed onto the camera but rather gets manipulated using a system of lenses. First, a simulation is performed to understand the behaviour of the system regarding the positioning of the components. This setup is then characterised in terms of magnification and resolution outside of the experiment. After the setup was integrated into the experiment the magnification was characterized again.

5.1 Requirements and constraints

To be able to design an imaging setup first the performance requirements as well as the constraints on the setup must be defined:

- It should be possible to image atoms in an MOT as well as a BEC. In terms of magnification, $M \approx 1$ and $M \approx 5$ should be reachable. This can be achieved by adding, respectively removing, lenses from the system. This mechanism should be realized in a way that does not require an extensive alignment procedure when switching between these two modes.[1]
- The setup should be diffraction limited. For the BEC imaging a resolution of around 10 µm should be reached.
- Aberrations should be minimized.
- The system should be optimized for a wavelength of 421 nm as this wavelength corresponds to the imaging transition
- After passing through the atoms the imaging beam shares a beam path with another beam. They are separated by two dichroic mirrors after exiting the vacuum chambers. This adds a lower limit to the distance between the atoms and the first lens of about 400 mm.

[1] Simply using flip mounts is not possible because magnets are used within them. Any magnetic materials should not be used near the experiment as they will act on the Dysprosium atoms due to their large magnetic moment.

5.2 Imaging setup

The described requirements can be reached by using a four lens setup as shown in Figure 5.2.1. It consists of an outer telescope with a magnification of 1. The first lens with a focal length of $f_1 = 500\,\text{mm}$ is placed one focal length away from the atoms. Another lens with the same focal length $f_4 = f_1$ is placed 1 m behind the first lens. Between these lenses, an inner telescope is mounted. These two lenses are mounted on a small, movable breadboard so that they can be put in and out of the system without completely losing the alignment. The inner lenses have focal lengths of $f_2 = 500\,\text{mm}$ and $f_3 = 100\,\text{mm}$. The magnification in the four lens configuration is

$$M_4 = \frac{f_4}{f_1} \cdot \frac{f_2}{f_3} = 5 \tag{5.2.1}$$

as desired, in the two lens configuration it is

$$M_2 = \frac{f_4}{f_1} = 1. \tag{5.2.2}$$

In order to be able to switch the magnification from 5 to 1 one needs to be able to put the lenses L_2 and L_3 in and out of the system. The necessary optical alignment caused by this switch should be as low as possible. To realize this the inner lenses are put on a small separate breadboard. After the system has been aligned the ideal position of the breadboard is marked using two clamps. They are placed so that the position of the breadboard is completely fixed if it is aligned to the clamps but it is still possible to remove the breadboard.
The best possible resolution in this configuration can be approximated using the Rayleigh condition to be

$$Y \approx 0.61 \frac{421\,\text{nm}}{\sin\left(12.7\,\text{mm}/500\,\text{mm}\right)} = 10.1\,\mu\text{m}. \tag{5.2.3}$$

5.3 Simulation of the optical setup

The setup is simulated in Zeemax OpticsStudio in order to decide which lenses to use and to gain information on the positioning sensitivity of the components. For the lenses L_1, L_2 and L_4 the planoconvex lens LA1908-A may be used, alternatively, the AC254-500-A achromatic doublet lens could be used. For the element L_3 the lenses LA1509-A or AC254-100-A can be used.[2]
Figure 5.3.1 shows the results of the simulations done with multiple configurations including simple planoconvex as well as achromatic lenses. The choice of the lenses

[2]All lenses mentioned here are bought from Thorlabs.

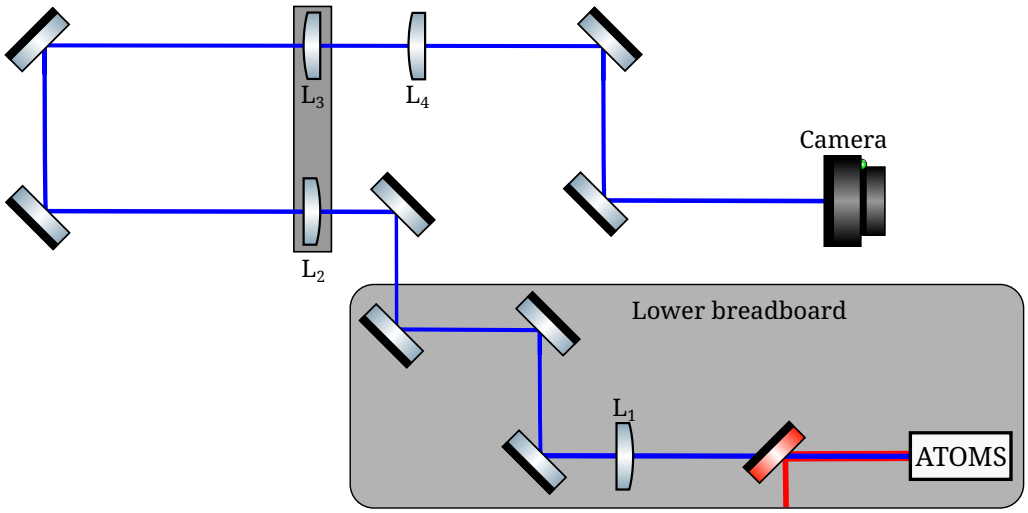

Figure 5.2.1: Drawing of the optical setup. The absorption imaging path shares a viewport of the vacuum chamber with another beam path. These beams are separated by a dichroic mirror, shown in read. The beam passes through the first lens L_1 and is guided onto an upper breadboard. It then passes through the lenses L_2 and L_3, which are mounted in parallel on a small, removable breadboard (light grey). Due to this construction, the magnification of the system can be changed by removing these two lenses. Afterwards, the beam passes through lens L_4 and is pointed onto the camera.

L_3 and L_4 does not significantly influence the results, the results for configurations where only these two lenses are changed to achromatic lenses are not shown in order not to make the analysis unnecessarily confusing. Replacing the lenses L_1 and L_2 with achromatic lenses does however change the performance of the system significantly. The only aberration present, even in the configuration without achromatic lenses, is spherical aberration. This can simply be inferred from the Seidel coefficients, which are not explicitly listed here as they are zero except for the coefficient S_1 shown in the bar chart in Figure 5.3.1, there is however also the possibility of using ray trace curves. They are computed by tracing rays through the exit pupil of the optical system. As a reference, the height on the image plane of the ray passing through the center of the pupil is taken. The deviation of rays passing through the outer parts of the exit pupil from this height is then plotted in dependence on a normalized pupil coordinate, which is basically the distance from the centre of the exit pupil normalized by the diameter of the pupil. The forms of these curves characterise the aberrations. A defocused system would for example exhibit a linear ray trace curve, spherical aberrations produce a third-order polynomial. The amplitude of these curves is a measure of the strength of these aberrations. [35]
As expected it is possible to significantly reduce the presence of spherical aberrations by using achromatic doublet lenses. Note that the reduction, or complete elimina-

tion, of spherical aberrations is not a normal property of achromatic lenses. They are usually designed to correct for chromatic aberrations. The achromatic doublet lenses by Thorlabs are however also optimized for the reduction of spherical aberrations. In theory aspheric lenses could have also been used to reduce aberrations. Using achromatic doublets has two main advantages: More focal lengths are available, especially for the necessary lenses with focal lengths of 500 mm, and they have a better off-axis performance than aspheres. This is especially relevant for taking images of the atom cloud when it is moving, e.g. falling under gravity, as the image will not be centered.

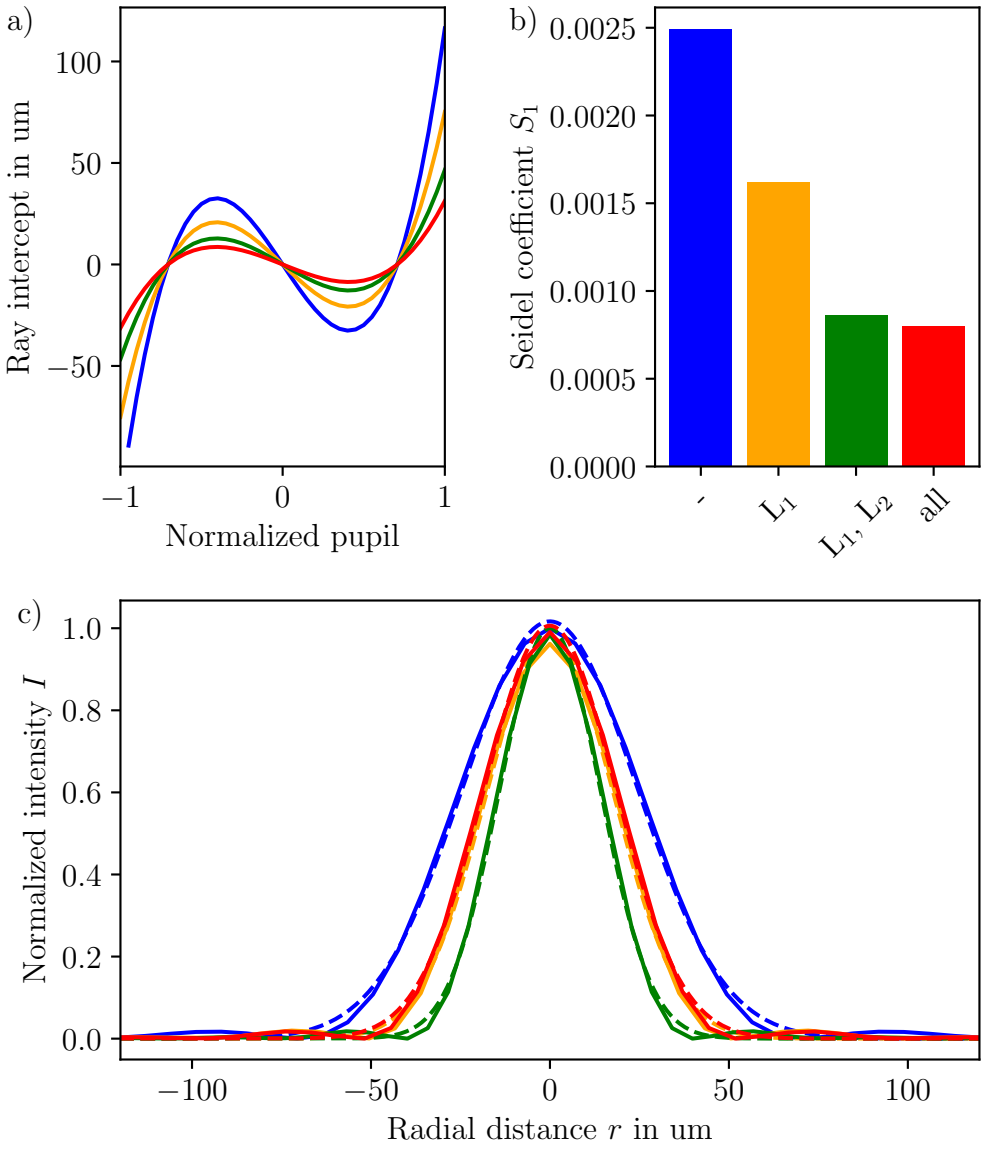

Figure 5.3.1: Simulation results for a configuration without achromatic lenses (blue), with the first lens (yellow), the first two lenses (green) and all lenses (red) replaced by achromatic lenses. **a)** Ray trace curves for the four setups. They have the form of a cubic polynomial, indicating the presence of spherical aberrations. The magnitude of this presence decreases drastically when the number of achromatic lenses is increased. **b)** The Seidel coefficient S_1 for all four setups. Replacing the first two lenses by achromatic lenses drastically decreases the presence of aberrations, the last two lenses do not have a significant influence. This confirms the conclusions drawn from a). **c)** The lower plot shows the PSFs for all four configurations as well as Gaussian functions (dashed lines) fitted to them. It can be seen that the width of the PSF can be significantly reduced by employing achromatic lenses. The fitted Gaussian functions describe the numerical PSF quite well, proving that the approximation of the PSF with Gaussian functions is justified for this system.

As for the sensitivity of the system to tilting, decentering or shifting the lenses L_3 and L_4 do not have a significant impact. The geometric spots within the airy disk, corresponding to the diffraction limit, are shown in Figures 5.3.2 and 5.3.3 for tilting the lenses L_1 and L_2 respectively. The maximum tilt with respect to the optical axis for the shown spots is 0.5°. However, even for these small tilts, the performance of the system is drastically decreased. Starting at tilts of 0.25° the system is no longer diffraction limited due to coma.

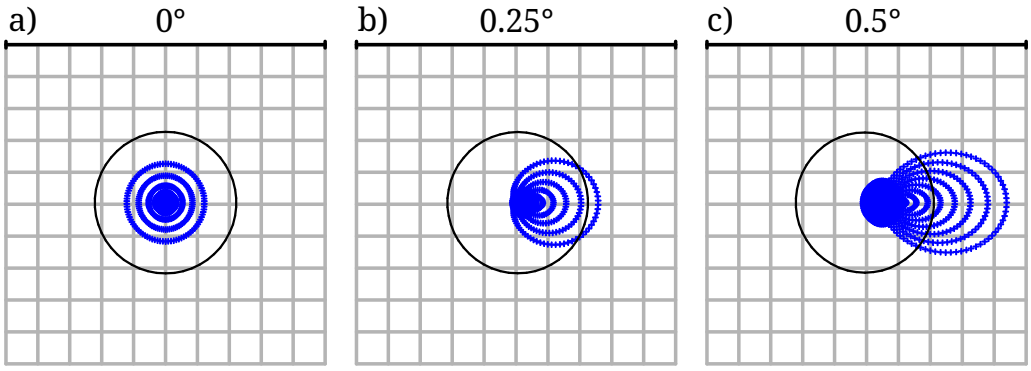

Figure 5.3.2: Simulated spots for tilts of a) 0°, b) 0.25° and c) 0.5° of the first lens. For the tilts shown in b) and c) the system is no longer diffraction limited. As described in Chapter 2.4 coma is occurring. The first minimum of the airy disk is shown as a black circle and the squares have side lengths of 20 µm

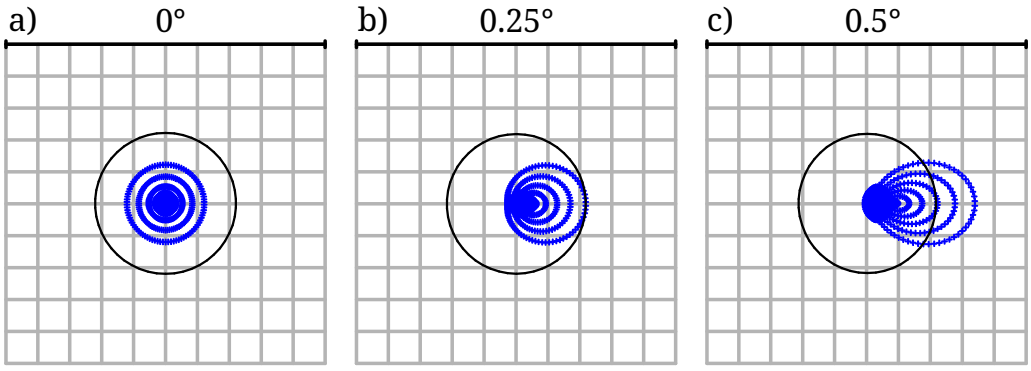

Figure 5.3.3: Simulated spots for tilts of a) 0°, b) 0.25° and c) 0.5° of the second lens. For a tilt of 0.25° the system is still diffraction limited, only for larger tilts this is no longer true.

Another degree of freedom is the position of the lenses relative to the object or to each other. Figure 5.3.4 shows the geometric spots for four variations of the distance between the point source and the first lens. Variations from the optimal distance by only 0.5 mm cause the system to no longer be diffraction limited. This can be compared to the theoretical depth-of-focus (DOF) by calculating the DOF using [14]

$$\mathrm{DOF} = \frac{\lambda \cdot n}{NA^2} = \frac{421\,\mathrm{nm} \cdot 1}{0.0254^2} = 0.65\,\mathrm{mm}. \tag{5.3.1}$$

Therefore the observations within the simulation agree with the theoretical prediction. For variations of the relative distance between the lenses L_2 and L_3, which is shown in Figure 5.3.5, this sensitivity to misplacement can also be found. In summary, it can be said that any misalignment of the first two lenses will heavily impair the performance of the system.

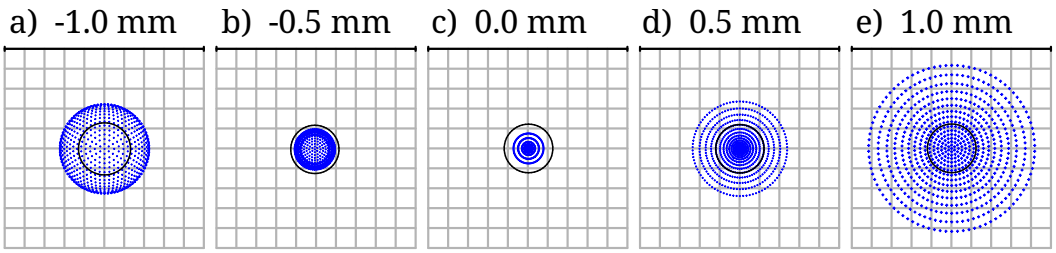

Figure 5.3.4: Simulated spots for moving the first lens a) 1 mm and b) 0.5 mm closer, as well as d) 0.5 mm and e) 1 mm away from the object. c) shows the spot for the optimited position. In the cases a), d) and e) the system is no longer diffraction limited. From this simulation it can be roughly estimated that the DOF is above 0.5 mm

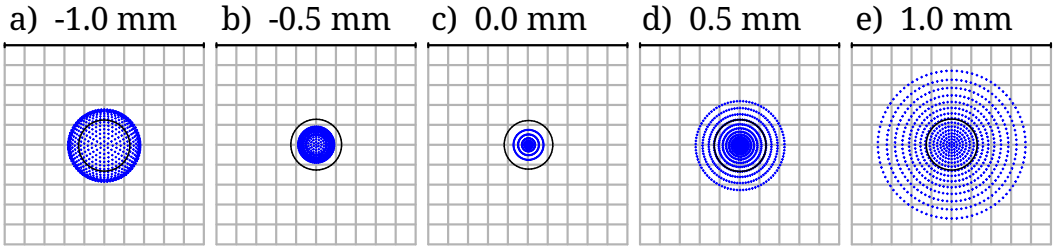

Figure 5.3.5: Simulated spots for increasing the distance between the second and third lens by a) 1 mm and b) 0.5 mm as well as decreasing it by c) 0.5 mm and d) 1 mm. c) shows the spot for the optimited position. In the cases a), d) and e) the system is no longer diffraction limited. This movement does not directly correspond to the DOF, it shows however that the resolution of the system is sensitive to the distance between the lenses L_2 and L_3.

5.4 Characterisation of the magnification and resolution

With the information obtained from the simulation, the setup is built up and coarsely aligned, by sending a collimated beam in and optimizing the outgoing beam to be again collimated. Then a 1951 USAF resolution test chart is placed in the object plane and imaged onto a camera. The optimized images are shown in Figure 5.4.1. The element 3 in group 1 consists of lines with a width of 198.43 µm and is used to determine the magnification. To do that the width in pixels is determined from an image, from which the magnification

$$M = \frac{459\ \text{px} \cdot 2.4\,\mu\text{m}}{198.43\,\mu\text{m}} = 5.55 \tag{5.4.1}$$

can be calculated. The resolution of the system can be estimated from the smallest still resolved group of lines. As element 6 from group 5 is still resolvable an upper limit to the resolution of 8.77 µm can be given.

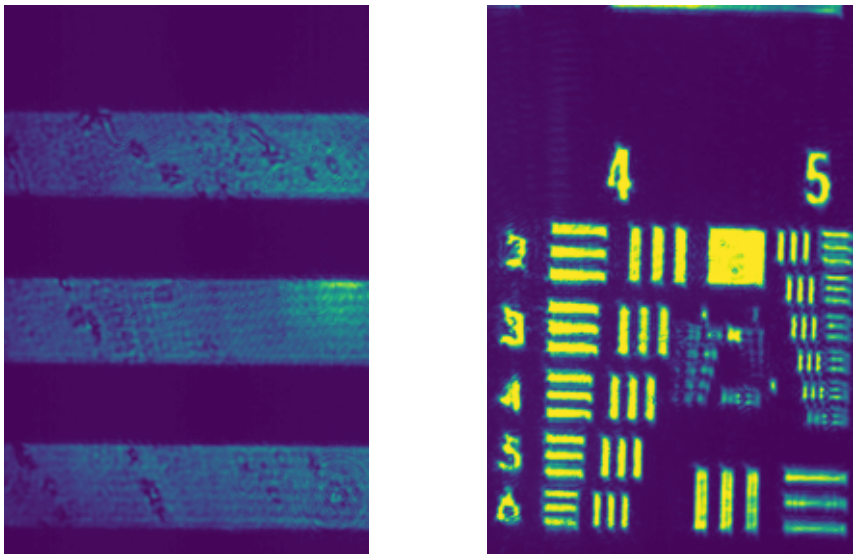

Figure 5.4.1: Images of a USAF resolution test chart. The left image shows element 3 from group 1, this image is used to determine the magnification of the system. The right image provides an overview of groups 4 and 5, used to estimate the resolution. Element 6 from group 5 (the smallest element from group 5), which is the smallest element with clearly distinguishable lines, corresponds to a resolution of 8.77 µm[36].

Another way of characterising the resolution of the system is by imaging circular apertures. The resulting intensity distribution is described by Equation (2.5.2). Figure

5.4.2 shows cuts in x- and y-direction of the intensity distribution of the image. By fitting (2.5.2) to these intensity profiles and setting the aperture diameter a to the value given by the used pinhole, the width w of the approximated PSF can be found. Note that the values obtained from the fit have to be divided by 5.55 to account for the magnification of the system. This method also allows some judgement on the presence of aberrations, as the resolutions in x- and y-direction should be equal, except when coma or astigmatism are present. The results of the fits are shown in Table 5.4.1. From these values resolutions in x- and y-direction of

$$w_\mathrm{x} = (11.5 \pm 0.2)\,\mu\mathrm{m} \quad \text{and} \quad w_\mathrm{y} = (10.0 \pm 0.2)\,\mu\mathrm{m} \tag{5.4.2}$$

can be found. Positioning these pinholes exactly at the same spot as the resolution test chart, to get the exact same measurement, as well as in the centre of the beam is not easily possible. Therefore some deviations between the resolution estimated from the test chart and this method are expected. In general, however, both methods prove that the imaging setup has a resolution on the order of 10 µm as needed. The deviations between w_x and w_y mainly stem from the measurement with a 20 µm pinhole. This pinhole might have been misplaced, some of the deviation may however also come from the aperture deviating from a circle. The minimal circularity of the aperture is specified to be 85% [37].

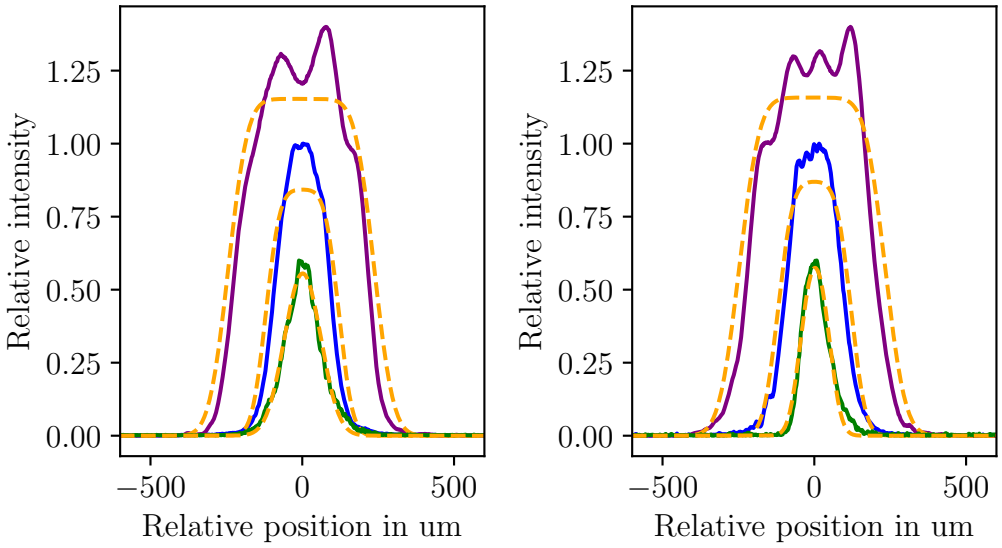

Figure 5.4.2: Intensity profiles of pinholes with aperture diameters of 20 µm (green), 50 µm (blue) and 100 µm (purple). Shown are cuts through the profile in x- and y-direction as well as fit functions according to Equation (2.5.4).

Table 5.4.1: Resolutions calculated from the fits shown in Figure 5.4.2.

Aperture diameter	$\mathbf{w_x}$	$\mathbf{w_x}$
20 µm	(13.3 ± 0.1) µm	(8.04 ± 0.05) µm
50 µm	(8.88 ± 0.13) µm	(9.39 ± 0.14) µm
100 µm	(12.4 ± 0.2) µm	(12.6 ± 0.3) µm

5.5 Characterisation of the magnification in the experiment

Characterisations like the ones shown in the previous chapter are not possible anymore when the setup is integrated into the experiment. The object plane is not accessible as it is situated in the vacuum chamber. Properties of the system can only be recovered by evaluating absorption images of atoms in the vacuum chamber.
Important for accurate recovery of the atom number is the magnification of the system. It is measured using a time of flight (ToF) measurement. Atoms are loaded into the MOT and then compressed into the compressed MOT (cMOT). The cMOT is turned off and the atoms fall down due to gravity. The ToF is therefore the time difference between turning of the cMOT and taking the absorption image. The center of mass of the atom cloud is determined from these images by fitting a Gaussian in x and y direction to them. By using the well known relation

$$\begin{pmatrix} x \\ y \end{pmatrix} = \frac{1}{2} \begin{pmatrix} a_\mathrm{x} \\ a_\mathrm{y} \end{pmatrix} t^2 \tag{5.5.1}$$

with the accelerations a_x and a_y in x and y direction. Note that the direction of gravitational force is not aligned with one of the image axis, therefore this two-dimensional equation has to be used. The magnitude of the acceleration vector is then the apparent gravitational acceleration. The results of ToF measurements in the two and four lens configuration are shown in the Figures 5.5.1 and 5.5.2. From the fits the accelerations

$$|\vec{a}_2| = (6.04 \pm 0.01)\,\frac{\mathrm{m}}{\mathrm{s}^2} \quad \text{and} \quad |\vec{a}_4| = (31.93 \pm 0.03)\,\frac{\mathrm{m}}{\mathrm{s}^2} \tag{5.5.2}$$

were found. These correspond to magnifications of

$$M_2 = 0.616 \pm 0.001 \quad \text{and} \quad M_4 = 3.25 \pm 0.01 \tag{5.5.3}$$

with the ratio of the magnifications being

$$\frac{M_4}{M_2} = 5.29. \tag{5.5.4}$$

With this method it is possible to precisely measure the magnification of the imaging setup, a necessary prerequisite for absorption imaging. From these measurements, however, large deviations to the theoretically expected magnifications are found. The

reasons for this is most likely an error in the placement of the first lens. As it is not easily possible to place it at the necessary distance to the atoms, this would need to be fixed by further alignment. For the further work done in this thesis, reaching the theoretical magnifications is not necessary, problems might only arise when trying to image a small BEC.

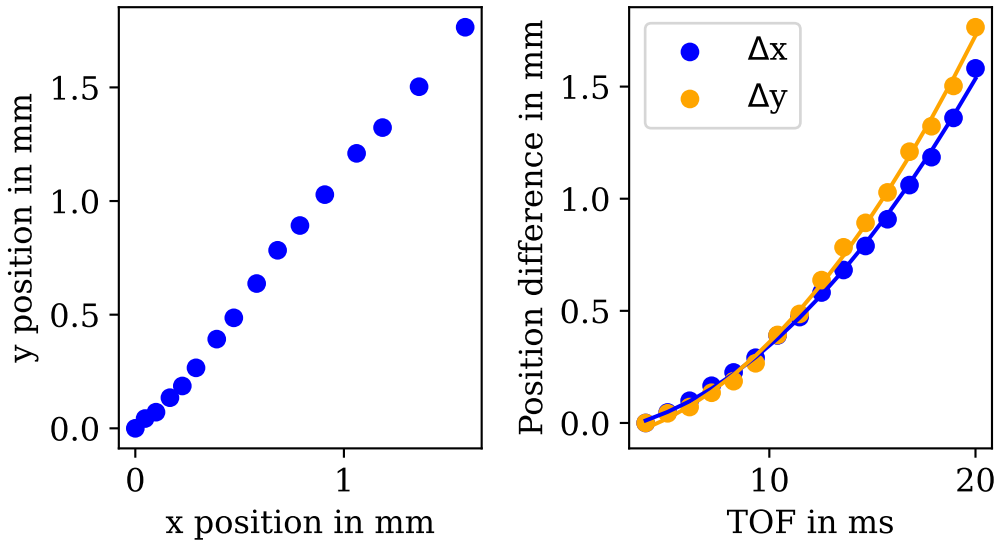

Figure 5.5.1: The left plot shows the position of the free falling atom cloud aquired by fitting Gaussian functions to absorption images taken in the two lens configuration with magnification M_2. Due to the optical elements the image is rotated, on the camera the cloud is moving in x-y-direction. The distance between the points is calculated and plotted against the time of flight. From two quadratic fits an acceleration of $(6.04 \pm 0.01)\,\mathrm{m/s^2}$ is found.

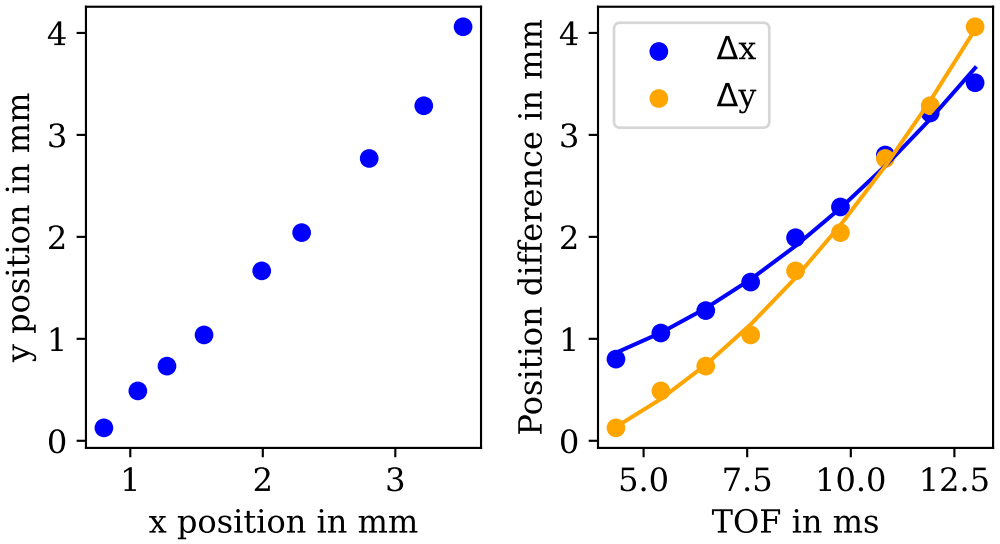

Figure 5.5.2: The left plot shows the position of the free falling atom cloud aquired by fitting Gaussian functions to absorption images taken in the four lens configuration with magnification M_4. Due to the optical elements the image is rotated, on the camera the cloud is moving in x-y-direction. The distance between the points is calculated and plotted against the time of flight. From two quadratic fits an acceleration of $(31.92 \pm 0.03)\,\mathrm{m/s^2}$ is found.

6 Experimental results

In this chapter the experimental results of performing absorption imaging with wavelengths of 421 nm and 626 nm are presented. For the first wavelength it can be shown that, under the circumstances in the experiment, high-intensity corrections do not need to be accounted for. The transition at 626 nm is used to illustrate the effects of imaging at and above saturation.

6.1 Imaging with $\lambda = 421\,\mathrm{nm}$

The transition employed for absorption imaging in the experiment is located at 421 nm and has a large natural linewidth of $\Gamma = (31.9 \pm 0.8)\,\mathrm{MHz}$. [22] From this linewidth a theoretical saturation intensity of $I_{\mathrm{sat}} = (88.9 \pm 2.4)\,\mathrm{W/m^2}$ results.
In Figure 6.1.1 the images necessary for performing absorption imaging are shown. First, an image with the imaging beam turned on is taken. On this image the absorption can already be seen as a shadow on the image. A reference image without atoms is also taken. In both images interference patterns can be seen. By dividing the absorption imaging through the reference image the optical density as seen in the third picture is found. If the time between the absorption and reference image is sufficiently short, the interference patterns do not move and cancel out in this division. In the case shown a lot of these patterns cancel out, however some finer patterns are still visible on the plot of the optical density.
With the laser power available in the experiment it was not possible to perform high intensity imaging. Figure 6.1.2 shows the atom densities calculated from absorption images at saturations on the order of less than 10%. The atom number fluctuates heavily, which is however not a result of the imaging but from the preparation of the cloud. To compensate for these effects a Savitzky-Golay filter with a window length of 20 and a polynomial order of 1 is applied, shown as dashed lines. From this data some dependence on the intensity can be found: At the lowest imaging intensity the calculated atom number is reduced by 1.3% due to saturation effects, at the highest intensity it is reduced by 4.7%. Therefore some dependency on the imaging intensity can be seen. Due to the large fluctuations of the atom number extracting quantitative information from this data is complicated and it would be necessary to go to higher intensities, so that the effects caused by saturation become larger, or at least comparable, to the fluctuations of the atom number.
The data presented here was taken at significantly higher intensities than the absorption imaging usually performed in the experiment to try to illustrate effects occurring

at higher intensities. Even using these increased intensities the corrections to Beer's law are small, at significantly lower intensities they become negligible. On one hand this results is quite positive for the experiment in general, as no complicated calibrations are necessary. On the other hand for studying high-intensity effects, the aim of this thesis, this is quite impractical. A solution in form of switching to another transition is presented in the next chapter.

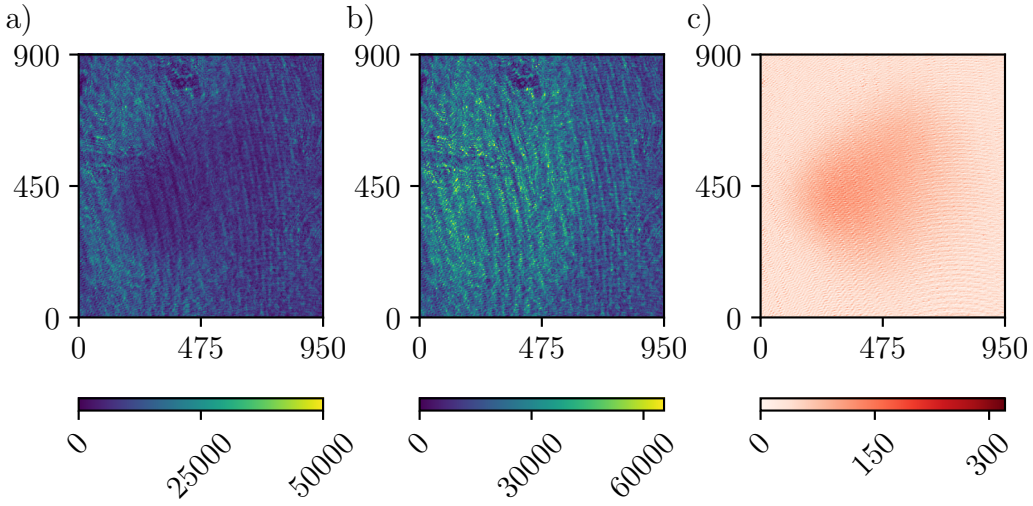

Figure 6.1.1: **a)** Absorption image of an atom cloud at a wavelength of 421 nm. The cloud can be identified as the shadow in the center region. **b)** Reference image taken under the same conditions as the absorption image, however no atoms are trapped. **c)** Atom density calculated from the absorption and the reference image by applying Equation (3.3.9). The atom number in the cloud can be calculated by summing the atom densities in this image up.

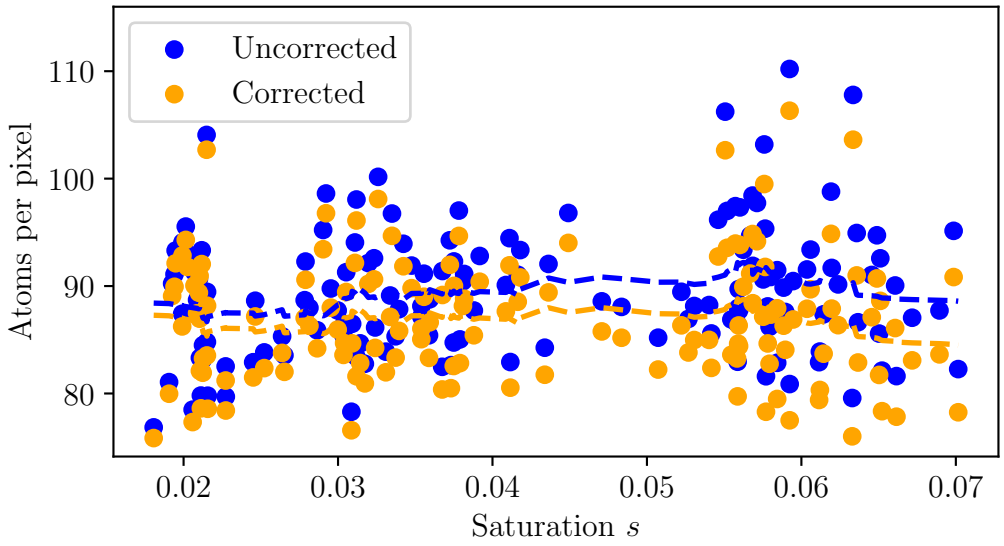

Figure 6.1.2: Atom densities calculated from absorption imaging with a wavelength of 421 nm. The uncorrected densities are calculated using Beer's law (3.3.2), the corrected densities take saturation into account according to Equation (3.3.9). The dashed lines are obtained from appliying a Savitzky-Golay filter with a window length of 20 and a polynomial order of 1. The difference between the corrected and uncorrected atom number increases for larger intensities. This effect is here however not large enough to quantitatively analyse and calibrate the imaging.

6.2 Imaging with $\lambda = 626\,\mathrm{nm}$

In contrast to the 421 nm transition the 626 nm has a small natural linewidth of (136 ± 4) kHz with a saturation intensity of $I_{\mathrm{sat}} = (115 \pm 4)\,\mathrm{mW/m^2}$.[38] It is therefore easily possible to use intensities significantly above saturation for imaging.

6.2.1 Power-broadening

As a first step the effective saturation intensity $I_{\mathrm{sat}}^{\mathrm{eff}}$ is determined by measuring the linewidth of this transition at multiple intensities. Figure 6.2.1 shows the absorption coefficient $\kappa(\omega)$ for 5 different intensities. A global shift away from the resonance at 626 nm is caused by the Zeeman effect as magnetic fields are present in the vacuum chamber. For higher intensities the transition saturates and the fraction of absorbed photons decreases. Therefore the linewidth of the transition decreases. By fitting the lineshape function (3.3.5) to the data sets
alpha 1.30(14) The linewidths $\Delta\omega_{\mathrm{FWHM}}$ extracted from these fits are shown in Figure 6.2.2 plotted over the intensity I. A fit according to equation (3.4.6) is fitted to the

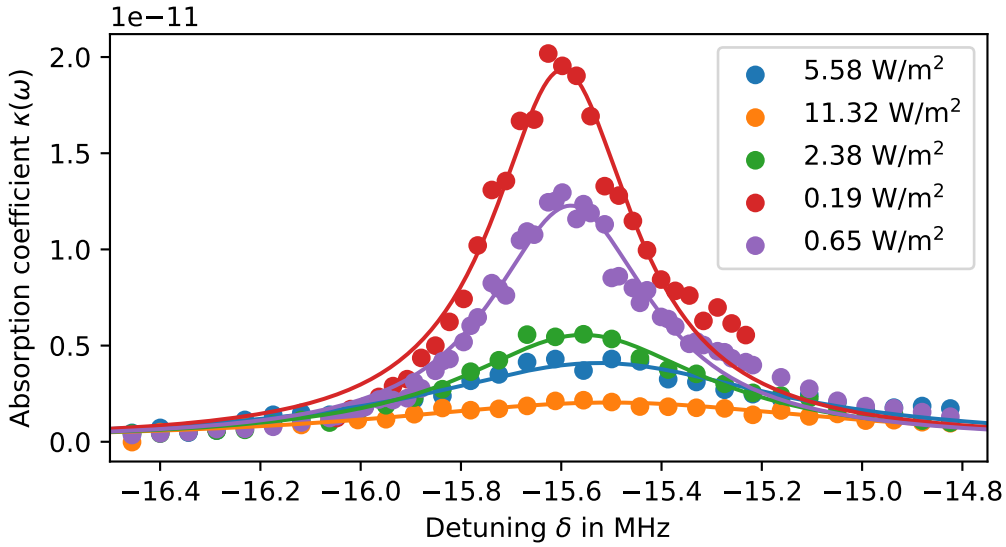

Figure 6.2.1: Power broadening of the 421 nm transition at multiple imaging intensities. The maximum of the absorption coefficient is located at a detuning of about $-15.6\,\mathrm{MHz}$ because the transition is shifted by the Zeeman effect. The lines are fits using equation (3.3.5), resulting in the linewidths $\Delta\omega_{\mathrm{FWHM}}$. The expected broadening of the profiles is clearly visible.

linewidths. The fit parameter is the correction factor α, which was determined to be

$$\alpha = 1.30 \pm 0.14. \tag{6.2.1}$$

Note that the aim of imaging this transition is to show the high intensity effects in absorption imaging and demonstrating that it is possible to correct them. Therefore this value was not determined in a way that would yield a highly precise value. For example, the camera was not calibrated for the used wavelength, rather the quantum efficiency was taken from the datasheet. The determined linewidths also deviate significantly from the fit function, especially for low intensities. In this range the linewidths should be close to the natural linewidth of 136 kHz, the measured values are significantly larger. This hints to the presence of additional broadening mechanisms in the sample.

6.2.2 Atom number reconstruction

At ten different intensities sets of absorption images are taken and the atom numbers are calibrated. The top right plot in Figure 6.2.3 shows the atom number calculated using Beer's law as purple circles. As all images were taken under similar conditions, except for the intensity of the imaging beam, the atom number within the clouds should be roughly the same, except for fluctuations. Therefore multiple measurements

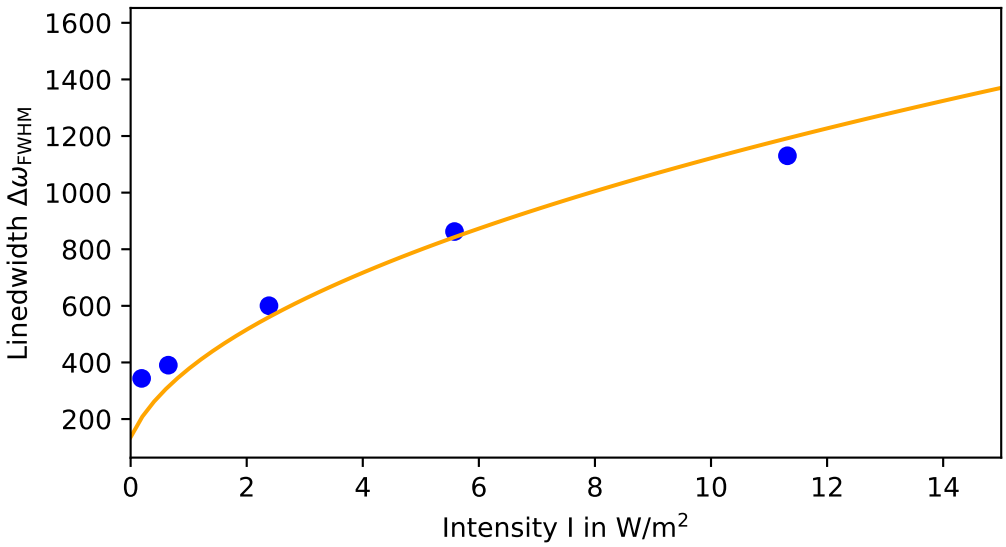

Figure 6.2.2: Linewidths $\Delta\omega_{\mathrm{FWHM}}$ extracted from the fits shown in Figure 6.2.1 in dependence of the saturation s. The orange line is a fit using Equation (3.4.6), from which the correction coefficient α can be determined to be 1.30 ± 0.14. For low intensities the determined linewidths are still significantly above the natural linewidth $\Gamma = 136\,\mathrm{kHz}$, which might indicate the presence of further broadening mechanisms.

at one intensity are taken and averaged, to reduce the influence of fluctuations. It is clearly visible that the calculated atom number is heavily dependent on the imaging intensity. Therefore the correction term is taken into account, which in theory should reduce the variance σ of the calculated atom numbers. Especially the variance should be minimal for the effective saturation intensity measured in the previous chapter. This was not the case for this measurement, as is shown in the top left figure. The atom numbers were calculated for multiple values of the correction parameter α, the minimum of the variance was found at $\alpha = 8.67$. The atom number calculated with this value are shown as green crosses in the large plot as well as in the top right plot compared to the uncorrected atom number. It is clearly visible that the variance of the atom number can be greatly reduced. For the shown calculations the scattering cross section σ_0 is used, which is not corrected for the Doppler shift. A numerical calculation as presented in Section 3.6 for the properties of the 626 nm however shows that the influence of the Doppler shift is completely negligible. Even for the largest calculated correction factor $1 - \gamma < 1.3 \cdot 10^{-12}$ holds true. In order to find out if this value of α is really the correct one or is caused by errors in the measurements or calculations it would be possible to perform a much more extensive calibration process. Firstly, the calibration factor can be determined by a second, independent method. As the momentum transfer is also dependent on the saturation intensity measuring the acceleration of the cloud parallel to the imaging beam yields α, see [39] for a

detailed description. Secondly, in [40] a calibration process using the here presented variance minimization process is shown, which is however done for multiple different atom densities. This allows for a comparison with a theoretical model, also presented in [40], going beyond the single-atom description of the absorption process given in this thesis. As this transition will not be used further to do absorption imaging, no further calibration is done in this thesis.

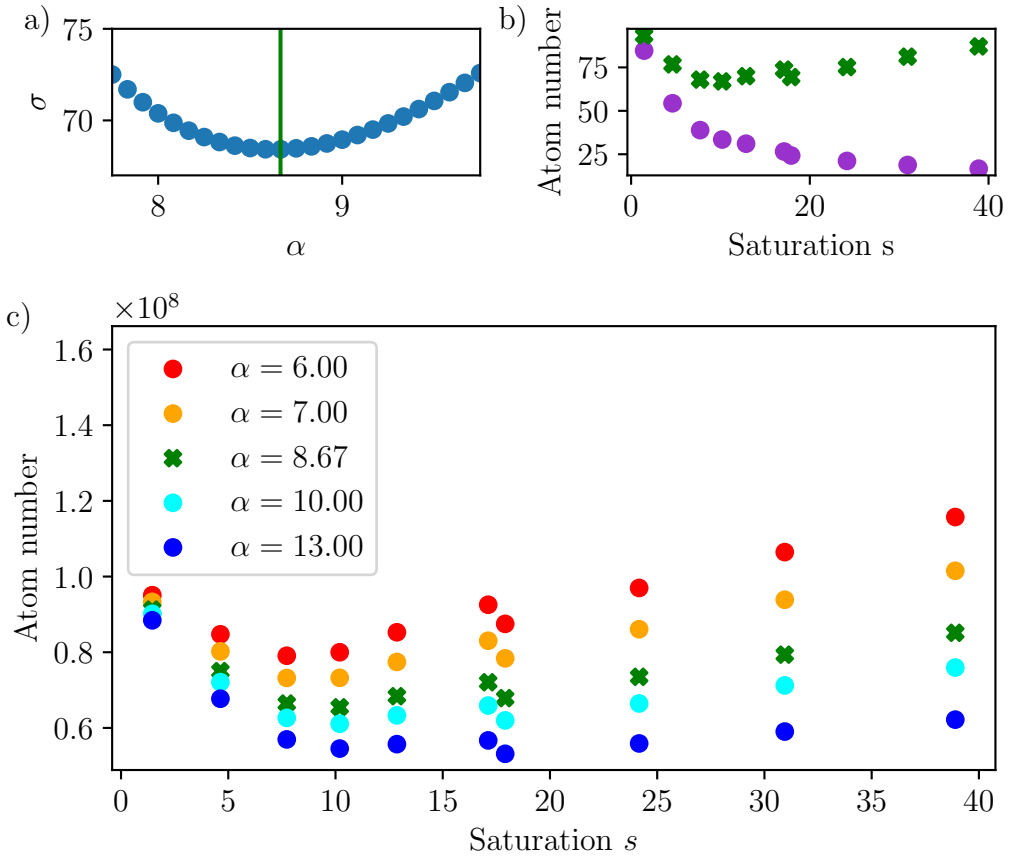

Figure 6.2.3: **a)** The variance σ of the atom number can be reduced by varying the correction parameter α. There is an optimum, at which the variance has a global minimum, the chosen value is marker with a vertical green line. **b)** The top right plot shows the uncorrected atom density in purple. It is heavily dependent on the imaging intensity. The green crosses show the corrected atom density. In this case it is still not constant, indicating that there might be another problem in the imaging process. However, the deviations of the density are greatly reduced by taking saturation of the transition into account. **c)** By choosing different parameters α it is possible to change the dependence of the atom number on the imaging intensity. Atom numbers calculated using a wide range of correction parameters are show, none of them, however, manages to produce a constant atom number.

7 Scheme for setting up an absorption imaging system

In this chapter a short guide to setting up an an absorption imaging system is given. What has been done concretely in the previous chapter is being presented in form of a checklist. Therefore additional absorption imaging setups can be integrated into the experiment in a much shorter time.

1. Define the performance requirements and operating conditions
   - At which wavelength will the imaging be performed, what is the natural linewidth of the corresponding transition?
     $\rightarrow$ Find the scattering cross section and saturation intensity.
   - What are the expected atomic densities?
     $\rightarrow$ At intermediate densities imaging at $s \approx 0.8$ or smaller is optimal. For higher intensities it may be necessary to use higher intensities to achieve a sufficient signal-to-noise ratio on the camera. In this case the Doppler shift during the imaging should be evaluated (see Chapter 3.6).
2. Characterise the used camera
   - The gain is calibrated by illuminating the camera uniformly and calculating mean and variance of these images at multiple intensities. The variance is directly proportional to the mean with the proportionality constant being the inverse gain.
   - For the quantum efficiency focus a laser beam at the wavelength used in the absorption imaging. Measure the power in the beam. Convert the count numbers of the image into primary electrons using the previously calibrated gain and sum them up to get the total number of generated photoelectrons. Divide this by the number of photons incident onto the chip during the exposure time.
3. Design and set up the optical setup
   - Optimize the setup to achieve the desired resolution and magnification
   - Calibrate the magnification by measuring the free fall of an atom cloud. By comparing the acceleration calculated from these images to the gravitational acceleration the magnification can be found.

4. Calibrate the atom number
    - The effective saturation intensity can be found from the power broadening. Determine the line width of the transition, preferably at intensities at or above saturation, then use Equation (3.4.6).
    - Take sets of images at multiple intensities. If the calculated atom number is dependent on the intensity the correction factor needs to be adapted to minimize the variance of the atom number

8 Conclusion & Outlook

In this thesis the process of setting up an absorption imaging setup for a cloud of Dysprosium atoms was covered from the theoretical foundations to the application. It was theoretically shown that depending on the density of the cloud and the imaging intensity significant deviations from Beer's law, which is usually used to calculate the densities, occur.

In a first step two scientific CCD cameras where characterised to enable the conversion of counts in the image to intensities. The BFS-U3-63S4M-C camera was found to have an on-chip gain of $g = 0.21 \pm 0.01 \frac{\mathrm{e}^-}{\mathrm{ADU}}$ with a quantum efficiency of $QE = 0.70 \pm 0.02$ at a wavelength of 421 nm. For the BFS-U3-70S7M camera the on-chip gain was determined to $g = 0.33 \pm 0.01 \frac{\mathrm{e}^-}{\mathrm{ADU}}$ with a quantum efficiency of $QE = 0.44 \pm 0.02$. For the imaging conditions used in absorption imaging the dark current and read noise were found to be negligible. Two EMCCD cameras, which offer the possibility of detecting up to single photons, are characterized to determine their suitability for use in a quantum gas microscope. From dark images, the distribution of count values is calculated and the gain as well as the read noise is extracted from these histogramms. For the Andor iXon Ultra 888 EMCCD camera the highest reachable gain over read-noise ratio was found to be $g/\sigma_{\mathrm{read}} = 57.41$, corresponding to an extraction fidelity of 86.99% at a threshold of $8\sigma_{\mathrm{read}}$. This allows single photon detection, especially as the performance might be enhanced even more by employing water cooling. The Andor iXon 3 EMCCD camera was only able to reach a gain over read-noise ratio of at most $g/\sigma_{\mathrm{read}} = 18.59 \pm 0.23$ with an extraction fidelity of 65.03%, which is below the performance needed for single photon detection.

In the second step toward performing absorption imaging an optical setup with a magnification switchable between 1 and 5 was designed. Using a simulation it was shown that, using achromatic lenses, it is possible to optimize the system to be diffraction limited with a resolution of around 10 µm. A test setup was assembled and characterized. The magnification of this system was measured to be $M = 5.55$ at a resolution of 8.77 µm using a USAF resolution test chart. By imaging pinholes, the resolution was again determined, this resulted in a value of (10.7 ± 0.2) µm slightly above the value inferred from the test chart. Lastly, the setup was integrated into the experiment and time of flight measurements with free falling atom clouds were done to again measure the magnification. In the two lens configuration, it was found to be $M_2 = 0.616 \pm 0.001$, in the four lens configuration it is $M_4 = 3.25 \pm 0.01$, deviating from the theoretical values.

With this setup absorption imaging at 421 nm is performed, it is however not possible

to reach saturations larger than $s = 0.1$ with the laser power available. Using the modified Lambert-Beer law corrections on the order of a few percent arise. Calibrating the calculation of the atom number is not possible at these intensities, it is however also not necessary.

The calibration of high intensity absorption imaging can be demonstrated using imaging light at a wavelength of 626 nm, the corresponding transition in Dysprosium has a small natural linewidth, leading to a comparably small saturation intensity. Therefore it is possible to observe the power broadening of this transition and determining the effective saturation intensity to $I_{\mathrm{sat}}^{\mathrm{eff}} = (1.30 \pm 0.14) I_{\mathrm{sat}}$. Then multiple sets of absorption images are taken and the atom number is calculated from them for multiple values of the correction factor α. By minimizing the variance of the atom number a correction factor of $\alpha = 8.67$ is determined. Contrary to the theoretical prediction it was not possible to completely eliminate the dependence on the intensity.

Within this thesis, the steps necessary for setting up and calibrating a high intensity absorption imaging system were described. It was found that under the conditions present in the experiment corrections caused by saturation effects do not significantly change the reconstructed atom number. This thesis can however be used as a guideline for future absorption imaging of BECs or quantum droplets, in which, due to their high density, the described corrections will be significant. In these situations again absorption images using multiple different imaging intensities need to be taken and the determination of the correction factors needs to be repeated. Additionally for precisely reconstructing the atom number of small structures the four lens setup needs to be used, which has not yet been done. Only these measurements will reveal the performance of the designed setup under real experimental conditions.

Further improvements to the implemented imaging setup can be made in the processing of the taken images. Fringe removal algorithms are capable of reducing the noise in the calculated density distributions. The increased noise is caused by differences between the light distributions in the absorption and the reference image. A fringe removal algorithm calculates an ideal reference image out of the fringe pattern on the absorption image, decreasing or even completely eliminating fringes in the final picture.

9 Bibliography

[1] N. Bose. "Plancks Gesetz und Lichtquantenhypothese". In: *Zeitschrift fr Physik* 26.1 (1924), pp. 178–181. ISSN: 1434-6001. DOI: 10.1007/BF01327326.

[2] A. Einstein. *Quantentheorie des einatomigen idealen Gases*. Marilee E. Thomas and Robert C. Thomas Science and Related Subjects Collection Bd. 1. Verlag der Akademie der Wissenschaften, in Kommission bei Walter de Gruyter u. Company, 1924.

[3] M. H. Anderson et al. "Observation of Bose-Einstein Condensation in a Dilute Atomic Vapor". In: *Science* 269.5221 (1995), pp. 198–201. ISSN: 00368075.

[4] K. B. Davis et al. "Bose-Einstein condensation in a gas of sodium atoms". In: *Physical review letters* 75.22 (1995), pp. 3969–3973. DOI: 10.1103/PhysRevLett.75.3969.

[5] NobelPrize.org. *The Nobel Prize in Physics 2001*. 2023. URL: https://www.nobelprize.org/prizes/physics/2001/press-release/ (visited on 07/21/2023).

[6] A. Griesmaier et al. "Bose-Einstein condensation of chromium". In: *Physical review letters* 94.16 (2005), p. 160401. DOI: 10.1103/PhysRevLett.94.160401.

[7] M. Schmitt et al. "Self-bound droplets of a dilute magnetic quantum liquid". In: *Nature* 539.7628 (2016), pp. 259–262. DOI: 10.1038/nature20126.

[8] L. Chomaz et al. "Quantum-Fluctuation-Driven Crossover from a Dilute Bose-Einstein Condensate to a Macrodroplet in a Dipolar Quantum Fluid". In: *Physical Review X* 6.4 (2016). DOI: 10.1103/PhysRevX.6.041039.

[9] D. Baillie et al. "Self-bound dipolar droplet: A localized matter wave in free space". In: *Physical Review A* 94.2 (2016). ISSN: 2469-9926. DOI: 10.1103/PhysRevA.94.021602.

[10] J. Hertkorn et al. "Pattern formation in quantum ferrofluids: From supersolids to superglasses". In: *Physical Review Research* 3.3 (2021). DOI: 10.1103/PhysRevResearch.3.033125.

[11] Tilman Esslinger. "Fermi-Hubbard Physics with Atoms in an Optical Lattice". In: *Annual Review of Condensed Matter Physics* 1.1 (2010), pp. 129–152. ISSN: 1947-5454. DOI: 10.1146/annurev-conmatphys-070909-104059.

[12] Immanuel Bloch, Jean Dalibard, and Wilhelm Zwerger. "Many-body physics with ultracold gases". In: *Reviews of Modern Physics* 80.3 (2008), pp. 885–964. ISSN: 0034-6861. DOI: 10.1103/RevModPhys.80.885.

[13] W. Demtröder. *Experimentalphysik 2: Elektrizität und Optik*. 7., korr. und erw, Auflage 2017. Springer-Lehrbuch. Berlin, Heidelberg: Springer Berlin Heidelberg, 2017. ISBN: 9783662557907.

[14] M. Born and E. Wolf. *Principles of optics: Electromagnetic theory of progagation, interference and diffraction of light*. 7th (expanded) ed. Cambridge (US): Cambridge University Press, 2009. ISBN: 9780521642224.

[15] E. Hecht, ed. *Optik*. 7. Auflage. De Gruyter Studium. Berlin and Boston: De Gruyter, 2018. ISBN: 9783110526653. DOI: 10.1515/9783110526653.

[16] V. N. Mahajan. *Optical imaging and aberrations*. Bellingham, Wash.: SPIE Optical Engineering Press, 2013. ISBN: 9780819425157. DOI: 10.1117/3.265735.

[17] F. Träger. *Springer handbook of lasers and optics: With 163 tables*. 2. ed. Berlin and Heidelberg: Springer, 2012. ISBN: 3642194087.

[18] H. Gross et al., eds. *Aberration Theory and Correction of Optical Systems*. Vol. / ed. by Herbert Gross ; Vol. 3. Handbook of optical systems. Weinheim: Wiley-VCH, 2007. ISBN: 9783527699254. DOI: 10.1002/9783527699254.

[19] C. J. Foot. *Atomphysik*. Berlin, Boston: De Gruyter Oldenbourg, 2011. ISBN: 9783110669121. DOI: 10.1515/9783110669121.

[20] K. Hueck et al. "Calibrating high intensity absorption imaging of ultracold atoms". In: *Optics Express* 25.8 (2017), pp. 8670–8679. ISSN: 1094-4087. DOI: 10.1364/OE.25.008670.

[21] R. Klemt. "Many-body correlations in a quasi-two-dimensional, ultracold atomic Fermi gas". Masterarbeit. Heidelberg: Universität Heidelberg, 2016. (Visited on 06/14/2023).

[22] M. Lu, S. H. Youn, and B. L. Lev. "Spectroscopy of a narrow-line laser-cooling transition in atomic dysprosium". In: *Phys. Rev. A* 83.1 (2011). DOI: 10.1103/PhysRevA.83.012510.

[23] M. Horikoshi et al. "Appropriate Probe Condition for Absorption Imaging of Ultracold 6Li Atoms". In: *Journal of the Physical Society of Japan* 86.10 (2017), p. 104301. DOI: 10.7566/JPSJ.86.104301.

[24] M. J. Howes and D. V. Morgan, eds. *Charge-coupled devices and systems*. Corrected reprint. Wiley-Interscience publication. Chichester [England] and New York: Wiley, 1980. ISBN: 0471996653.

[25] G. C. Holst. *CCD arrays, cameras, and displays*. 2. ed. Bellingham, Wash.: SPIE Optical Engineering Press, 1998. ISBN: 0964000040.

[26] M. Newberry. *Tech Note: Pixel Response Effects on CCD Camera Gain Calibration*. URL: https://www.mirametrics.com/tech_note_ccdgain.php (visited on 07/14/2023).

[27] FLIR. *BFS-U3-63S4M-C document package*. 2022. URL: https://www.flir.eu/support-center/iis/machine-vision/knowledge-base/technical-documentation-blackfly-s-usb3/.

[28] FLIR. *BFS-U3-70S7M document package*. 2022. URL: https://www.flir.eu/support-center/iis/machine-vision/knowledge-base/technical-documentation-blackfly-s-usb3/.

[29] ANDOR Technology. *What is an EMCCD Camera?* URL: https://andor.oxinst.com/learning/view/article/electron-multiplying-ccd-cameras (visited on 07/14/2023).

[30] K. B. W. Harpse, M. I. Andersen, and P. Kjgaard. "Bayesian photon counting with electron-multiplying charge coupled devices (EMCCDs)". In: *A&A* 537 (2012), A50. DOI: 10.1051/0004-6361/201117089.

[31] E. Lantz et al. "Multi-imaging and Bayesian estimation for photon counting with EMCCDs". In: *Monthly Notices of the Royal Astronomical Society* 386.4 (2008), pp. 2262–2270. ISSN: 0035-8711. DOI: 10.1111/j.1365-2966.2008.13200.x.

[32] Andrea Bergschneider et al. "Spin-resolved single-atom imaging of ^{6}Li in free space". In: *Phys. Rev. A* 97 (2018), p. 063613. DOI: 10.1103/PhysRevA.97.063613. URL: https://link.aps.org/doi/10.1103/PhysRevA.97.063613.

[33] ANDOR Technology. *iXon3 Hardware Guide*. 2011. URL: https://andor.oxinst.com/downloads/uploads/iXon3_Hardware_Guide.pdf.

[34] ANDOR Technology. *iXon Ultra & Life 888 Hardware Guide*. 2022. URL: https://andor.oxinst.com/downloads/uploads/Hardware_Guide_iXon_Ultra_Life_888.pdf.

[35] Robert Edward Fischer, Biljana Tadic-Galeb, and Paul R. Yoder. *Optical system design*. 2. ed. Vol. 176. SPIE PM. New York: McGraw-Hill, 2008. ISBN: 0071472487.

[36] *Resolution Test Targets*. 2023. URL: https://www.newport.com/f/resolution-test-targets (visited on 07/22/2023).

[37] ThorLabs. *Circular Precision Pinholes, Stainless Steel Foils*. URL: https://www.thorlabs.com/newgrouppage9.cfm?objectgroup_id=14350&pn=P20D (visited on 07/26/2023).

[38] M. Gustavsson et al. "Lifetime measurements for excited states of rare-earth atoms using pulse modulation of a cw dye-laser beam". In: *Journal of the Optical Society of America* 69.7 (1979), p. 984. ISSN: 0030-3941. DOI: 10.1364/JOSA.69.000984.

[39] G. Reinaudi et al. "Strong saturation absorption imaging of dense clouds of ultracold atoms". In: *Optics Letters* 32.21 (2007), pp. 3143–3145. ISSN: 1539-4794. DOI: 10.1364/OL.32.003143.

[40] Romain Veyron et al. "Quantitative absorption imaging: The role of incoherent multiple scattering in the saturating regime". In: *Physical Review Research* 4.3 (2022). DOI: 10.1103/PhysRevResearch.4.033033.